# High Entropy Boride-SiC Composite: Synthesis, Characterization and Thermo-oxidative behaviour

Rahul Mitra[1], Subhra Sourav Jana[1], Thiruvenkatam Venkateswaran[2], Chanchal Ghosh[3], Tanmoy Maiti[1], Krishanu Biswas[1]*

[1]*Department of Materials Science and Engineering, Indian Institute of Technology, Kanpur, Uttar Pradesh, India – 208016.*

[2]*Vikram Sarabhai Space Centre (VSSC), ISRO, Trivandrum 695022, Kerala, India.*

[3]*Materials Synthesis and Structural Characterisation Section, Physical Metallurgy Group, Indira Gandhi Centre for Atomic Research, Kalpakkam 603102, India.*

**Abstract:**

Silicon carbide reinforced multicomponent high entropy diboride-based particulate composites (HEB-SiC) were fabricated by spark plasma sintering at 1800°C using diboride powders prepared from boro-carbothermal reduction method to investigate the influence of the addition of SiC (SiC content = 20, 40 vol%) on the microstructural evolution, oxidation, and exposure to arc-jet behaviour was reported. SiC has been found to improve the densification of pristine diboride, with attainment of a maximum of ~ 98% relative density for SiC content of 40 vol%. A percolating network of SiC grains in the HEB matrix was observed in the case of composites with 40% volume fraction of SiC. The oxidative behavior at 1400°C in air revealed excellent improvement of oxidation resistance of 20 vol% SiC reinforced composite as compared to other sintered specimens. Arc-jet testing on 20 vol% SiC reinforced composite revealed no structural deformity with very minute-scaled formation of surface oxide layers. These results indicate that the addition of 20 vol% SiC in a diboride matrix can contribute to the optimal preparation of high entropy diboride-based ceramics with balanced mechanical properties with improved oxidation resistance.



https://doi.org/10.26434/chemrxiv-2024-pggps **ORCID:** https://orcid.org/0000-0002-3194-8561 Content not peer-reviewed by ChemRxiv. **License:** CC BY-NC 4.0

**Keywords:** High entropy diboride, silicon carbide, composites, thermal conductivity, oxidation behaviour.

*Corresponding author: Email: *kbiswas@iitk.ac.in*, Phone- +91-512-2596184, Fax: +91-512-2597505



https://doi.org/10.26434/chemrxiv-2024-pggps **ORCID:** https://orcid.org/0000-0002-3194-8561 Content not peer-reviewed by ChemRxiv. **License:** CC BY-NC 4.0

## 1. Introduction:

In recent years High entropy diborides (HEBs) have been considered an emerging class of materials in the field of ultra-high-temperature ceramics (UHTCs) [1-14]. These multicomponent materials were evolved utilizing the concepts derived from both the conventional UHTC materials and high entropy alloys (HEAs) [1]. These HEBs exhibit a unique combination of properties such as high melting temperature (>3000°C), high hardness (22.5-28.3 GPa), relatively higher fracture toughness (4.47±0.40 MPa•$m^{-1/2}$), chemical inertness, resistance to wear and corrosion, good electrical and thermal conductivities [1-4, 14]. Gild et al. first time synthesized a set of bulk HEBs synthesized *via* spark plasma sintering. The relative density achieved by the procedure was limited to ~92.4% [1]. Further, Zhang et al. developed another composition of HEB [$(Hf_{0.2}Mo_{0.2}Ta_{0.2}Nb_{0.2}Ti_{0.2})B_2$] synthesizing using borothermal reduction of the corresponding metal oxides at 2000°C and achieved a sinter density of ~98.5% [3]. The reported composition displayed an improved hardness ~27 GPa and fracture toughness ~4.47 MPa.$m^{-1/2}$. The research work done by Zhang et al. showed that HEB powder of the $(Hf_{0.2}Zr_{0.2}Ta_{0.2}Cr_{0.2}Ti_{0.2})B_2$ system, synthesized through borothermal reduction can achieve a much higher sinter density within the range of 95.0 ~ 99.2% [5]. Whereas the HEB powder synthesized utilizing boro/carbothermal route could reach a relative sinter density of 96.3% ~ 98.5%. They also showed the reported composition with nearly full densification can achieve remarkable hardness (28.3±1.6 GPa).

In addition to the enhanced physical properties, excellent mechanical, as well as thermomechanical properties, are also of increasing concern. In this regard, previous research on the development of fully sintered conventional UHTC materials ($ZrB_2$, $HfB_2$) directed the usage of secondary phases such as SiC, CNTs, $MoSi_2$, $TaSi_2$ to improve densification behaviour, mechanical properties as well as the oxidation resistance [15-19]. However, SiC has been reported to be best among them. Addition of SiC in different boride matrix have been



https://doi.org/10.26434/chemrxiv-2024-pggps **ORCID:** https://orcid.org/0000-0002-3194-8561 Content not peer-reviewed by ChemRxiv. **License:** CC BY-NC 4.0

investigated to improve the overall thermal conductivity by heat dissipation through the highly conducting SiC phase [20-22]. Additionally, the SiC in the boride matrix can also essentially improve the thermal shock resistance, which in turn can be expected to increase the dimensional stability of the composite material at high temperatures [23, 24]. In term of improving the oxidation resistance, SiC oxidises to form an adherent glassy layer of $SiO_2$ facilitating the smoother oxygen transport, thus reducing the oxidation of the pristine boride matrix [25]. In this context, the addition of SiC in the high entropy boride matrix can pose a significant improvement in the overall performance of the final composite. Few reports are available on the HEB-SiC system to reveal the effect of SiC addition in the high entropy boride matrix [26-28]. Studies reported by Shen et al. showed that the addition of SiC in $(Ti_{0.2}Zr_{0.2}Hf_{0.2}Nb_{0.2}Ta_{0.2})B_2$ can significantly improve not only the densification behavior but also can increase the fracture toughness by 30%. Further, Liu et al. investigated the addition of 20 vol% SiC in $(Ti_{0.2}Zr_{0.2}Hf_{0.2}Nb_{0.2}Ta_{0.2})B_2$ ceramic fabricated using hot pressing at 1800°C [27]. The corresponding results indicated a significant improvement in the four-point flexural strength, fracture toughness, and hardness ($Hv_{0.2}$) values from 339±17 MPa, 3.81±0.40 $MPa{\cdot}m^{1/2}$, and 23.7±0.7 GPa to 447±45 MPa, 4.85±0.33 $MPa{\cdot}m^{1/2}$, and 24.8±1.2 GPa, respectively. However, more studies are still required on HEB-SiC composite systems to fully understand the effect of powder processing and the addition of SiC addition on the densification behavior, mechanical and as well as thermophysical properties.

In the present investigation, self-synthesized HEB powder was mixed with different vol% of SiC and sintered using spark plasma sintering at much lower temperature (1800°C). The previously reported HEB ceramic system, namely $(Ti_{0.25}Zr_{0.25}Nb_{0.25}Cr_{0.25})B_2$ was chosen for the present study [14]. In particular, the bulk-HEBs were synthesized using boro-carbothermal reduction of oxides and were further ball- milled to powder. The influence of the addition of SiC on the densification, phase assemblage, microstructure, and thermos-oxidative



https://doi.org/10.26434/chemrxiv-2024-pggps **ORCID:** https://orcid.org/0000-0002-3194-8561 Content not peer-reviewed by ChemRxiv. **License:** CC BY-NC 4.0

behaviour of HEB-SiC ceramics was emphatically investigated and reported. Most importantly, in the present study the thermo-oxidative-structural stability of the composite ceramic has also been investigated via arc jet testing. These experimental results are finally correlated with the microstructure in order to find processing-microstructure-property relationship in the newly developed HEB-SiC system.

## 2. Experimental Procedure

### 2.1 Powder processing and consolidation by SPS

For the preparation of bulk ceramics, commercially available titanium oxide ($TiO_2$, Alfa Aesar, particle size ~520 nm; purity ~99.995%), niobium oxide ($Nb_2O_5$, Alfa Aesar, particle size ~770 nm; purity ~99.995%), zirconium oxide ($ZrO_2$, SRL, particle size ~930 nm; purity ~99.9%), chromium oxide ($Cr_2O_3$, Alfa Aesar, ~325 mesh purity ~98+%), boron carbide ($B_4C$, commercially available), and commercial α-SiC (purity > 98%, mean particle size of 700 nm) powders were used as initial powders. For synthesizing the HEB phase, all the oxide powders with equimolar ratio (according to the ratio of metals) were mixed with an appropriate concentration of $B_4C$ (5% extra). Subsequently, the powder batches were subsequently ball milled for 6 hours at 60 rpm in a planetary ball mill (Pulverisette5, Fritsch, Germany) using zirconia milling media with a ball to powder weight ratio (BPR) of 10:1 for mixing and reduction in the particle size.

The as-milled powder was further consolidated using the Spark Plasma Sintering machine (Dr. Sinter' 515 S, SPS Syntex Inc., Kanagawa, Japan). The reactive-SPS was carried out at 1800°C for 45 min (dwell time) with a heating rate of 100°C/min. under the flow of Ar (2L/min) to promote the formation of HEB *via* boro-carbothermal reactions. A uniaxial pressure of 18 MPa was used at the beginning of the compaction until 600°C to ensure the particle-particle contact, followed by the application of maximum pressure of 30 Mpa up to 1800°C,



https://doi.org/10.26434/chemrxiv-2024-pggps **ORCID:** https://orcid.org/0000-0002-3194-8561 Content not peer-reviewed by ChemRxiv. **License:** CC BY-NC 4.0

which was maintained throughout the sintering schedule (45 min). The sample was furnace cooled after the heating cycle was completed. The synthesized disc was then crushed and pulverized into fine HEB-powder. Further, the HEB powder was mixed with 20 and 40 vol% SiC and ball milled for 4 h at 100 rpm. The sample without SiC addition was labeled as HB and the sample with SiC addition was labeled as HBS20 and HBS40. The HBS20 and HBS40 powders were further densified by Spark Plasma Sintering machine at 1800°C for 30 min under vacuum level of $10^{-6}$ bar. A constant 30 MPa pressure was maintained during the dwell time.

The sintered pellet was ground and polished using different size grit paper (SiC paper: #80 to 2500) to obtain an asperity-free surface. The bulk density of the sintered pellets was measured using the Archimedes principle of buoyancy, where distilled water was used as a submersion medium by following ASTM B 962-17 standards. The measured densities are represented in Table 1. The progress of densification is explained in Section S1, Supplementary Information in a detailed manner.

**Table 1** Bulk density of the sintered specimen.

| Sample Name | Bulk density (g/cc) | Relative density (%) |
|---|---|---|
| HB | 4.98 | ~ 88% |
| HBS20 | 4.72 | ~ 92% |
| HBS40 | 4.61 | ~ 98% |

### 2.2 Characterization

The phase determination of the as-received powder, powder mixture, as well as the sintered sample, was carried out using X-ray Diffractometer (X-ray diffractometer, Empyron, PANalytical (45kV voltage, 40 mA current), USA) using Cu-kα radiation (λ = 0.15404 nm) over the range of 2θ from 20° to 80°, at a step size of 0.013 and a scan rate of 0.022°/sec. The



https://doi.org/10.26434/chemrxiv-2024-pggps **ORCID:** https://orcid.org/0000-0002-3194-8561 Content not peer-reviewed by ChemRxiv. **License:** CC BY-NC 4.0

morphological and compositional characteristics of the pellets were determined using scanning electron microscopy (SEM, Carl Zeiss EVO 50, Germany, and field emission scanning electron microscope, Nova Nano SEM-450, FEI, Netherlands) coupled with an energy dispersive X-ray spectrometer (EDS, Oxford Instruments, UK). To prepare the TEM sample of the composite specimens, at first, the 300 μm thick samples were cut in the form of a disc of 3 mm diameter using a spark erosion cutter (Wire Electric-Discharge Machine (EDM)) followed by the reduction in the thickness up to 100 μm by a dimple grinder (Model 656, Gatan, USA) to achieve an ultrathin sample (~30 μm) in the center region of the 3 mm disc. Subsequently, as-dimpled samples were ion milled (PIPS, Model 691, Gatan, USA) at 5 keV with 25 mA beam current and 5° milling, followed by ion milling at 2 keV at 2° after the perforation had been achieved. The fine-scale microstructural features were observed using a transmission electron microscope TEM (FEI Techni: 20 UT, USA (operated at 120 kV); and FEI TITAN 300 kV, Netherlands).

### 2.3 Thermal conductivity measurement

The thermal conductivity of the sintered samples (diameter of 12.5 mm and thickness of 2 mm) was measured by Laser Flash Apparatus (LFA 447 Nanoflash™system, NETZSCH, Germany) under argon atmosphere (1 atm) following the ASTM 1461 standard. A pulsed Nd:YAG laser was used for ~300 μs during the measurements. The laser flash method offers an indirect measurement of thermal conductivity by measuring the thermal diffusivity and further correlating it with the specific heat and density. The thermal diffusivity ($\alpha$) ($cm^2/s$) can be measured using the following equation,

$$\alpha = \frac{0.13879L^2}{t_{1/2}} \qquad (1)$$

The thermal diffusivity is related to thermal conductivity by the following relation:



https://doi.org/10.26434/chemrxiv-2024-pggps **ORCID:** https://orcid.org/0000-0002-3194-8561 Content not peer-reviewed by ChemRxiv. **License:** CC BY-NC 4.0

$$k_t = \alpha \rho C_P \qquad (2)$$

Where, where, $\rho$ is the measured density (g/cm$^3$), $C_P$ is the specific heat capacity [J·(mol·K)$^{-1}$] (simultaneously measured using laser flash diffusivity technique with an accuracy of ±5%). The measurements were conducted at 95% confidence with a coverage factor of k = 2. Furthermore, the thermal conductivity ($k_t$) was then corrected for the porosity using the following equation:

$$k = k_t \frac{(1+0.5P)}{(1-P)} \qquad (3)$$

where k is the total intrinsic thermal conductivity [W·(m·K)$^{-1}$], and $P$ is the volume fraction of porosity present in the samples. This was conducted for all the specimens.

### 2.4 Oxidation study

An oxidation study of the pristine HEB specimen and HEB-SiC composites was carried out in an open-air furnace by exposing the specimens to 1400°C for 1 h. The phase analysis of the oxidized surface was carried out using X-ray Diffractometer (X-ray diffractometer, Empyron, PANalytical (45kV voltage, 40 mA current), USA) using Cu-kα radiation (λ = 0.15404 nm) over the range of 2θ from 20° to 90°, at a step size of 0.013 and a scan rate of 0.022°/sec. The cross-sectional morphology and compositional study were determined using scanning electron microscopy (SEM, Carl Zeiss EVO 50, Germany, and field emission scanning electron microscope. The hardness along the cross-section of the oxidized samples were measured under 0.5N load, using a Vickers microhardness tester (CSM international, USA) following ASTM C 1327-15 standard and calculated using Equation 4.

### 2.5 Arc-Jet test

Arc-Jet test offers the ultimate ground based simulation of the re-entry conditions for the UHTC specimens. Based on the initial oxidation study at 1400°C, SPS sample with the best oxidation resistance using dimension of 15 mm diameter and 3 mm thickness was exposed to



https://doi.org/10.26434/chemrxiv-2024-pggps **ORCID:** https://orcid.org/0000-0002-3194-8561 Content not peer-reviewed by ChemRxiv. **License:** CC BY-NC 4.0

plasma-arc jet under the heat flux of 250 W/sq. cm. The heat flux was measured directly using a thin foil heat flux transducers (HFT) with a 5% margin of error. The plasma generator was fed with a mixture of air (78.1% $N_2$ and 20.9% $O_2$) and argon (~ 2%) at a flow rate of 3.62 g/s and the heated gas was discharged into the outside environment through a supersonic nozzle at Mach 1.4. The test specimen was placed in specific manner to achieve one-dimensional heating from the front face then subjected to an arc jet for 30 seconds. During the arc-jet test, the back wall temperature was measured using a *K*-type thermocouple attached using high temperature cement on the back face of the specimen. Water-cooled Gordon gauges were used in order to calibrate the requisite heat flux and other operational parameters.

## 3. Results and discussion

### 3.1 Phase assemblage study and microstructural investigation

The XRD patterns of the as-sintered samples of high entropy diboride and the composite specimens (HEB-SiC ceramics) are shown in Fig. 1a. For reference, the XRD pattern of as-received SiC powder is also represented along with the other patterns. The XRD pattern of the HB sample shows all the peaks belong to HEB phase; albeit no other secondary phases cannot be detected. From the XRD patterns of the composite samples in (Fig. 1a) shows that the high intense peaks in all the samples belong to the HEB phase owing to its presence at higher volume fraction (80 vol % and 60 vol %). In addition, the XRD patterns of HBS20 show diffraction peaks of α-SiC, however, the peak intensities are weak in comparison to that of the HEB phase. Meanwhile, in the case of HBS40, the diffraction peaks corresponding to α-SiC were found to be strong as compared to HBS20 owing to its higher volume fraction in the pre-sintered powder.



https://doi.org/10.26434/chemrxiv-2024-pggps **ORCID:** https://orcid.org/0000-0002-3194-8561 Content not peer-reviewed by ChemRxiv. **License:** CC BY-NC 4.0

The patterns denote that the HEB phase is stable during the SPS process and any undesirable peaks due to the interfacial reactions between HEB and SiC phases cannot be noticed.

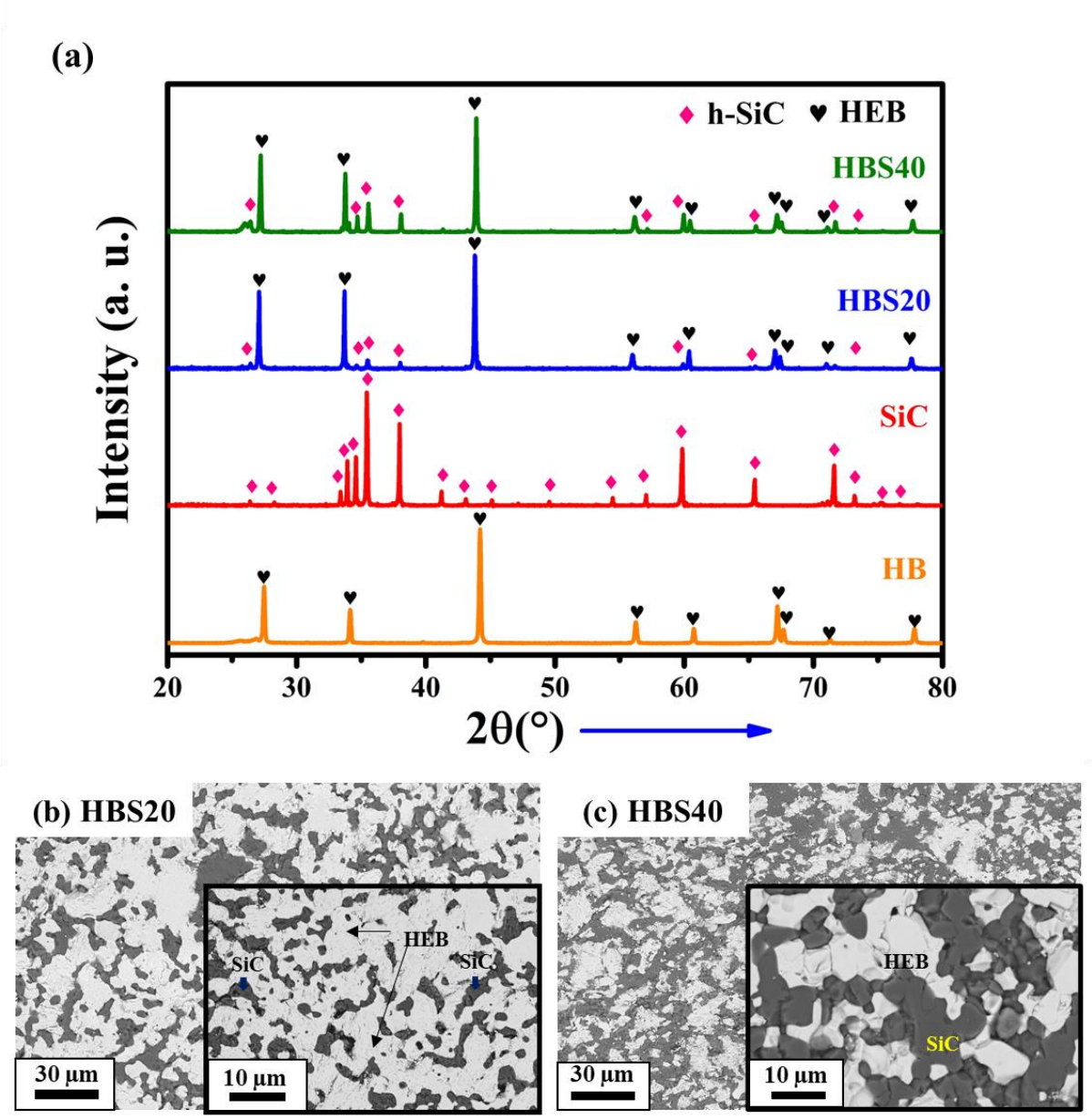


**Fig. 1 (a).** XRD patterns of the spark plasma sintered pellets revealing the evolution of phases in synthesized HEB powder, as-received SiC and HEB-SiC composites (vol%= 20, 40). BSE-SEM micrographs of the polished surface of HEB-SiC composites showing different phases with distinct contrasts **(a)** HBS20, **(b)** HBS40.

Further, the cross-sectional BSE-SEM images of the HBS20 and HBS40 composites are presented in Fig. 1b and 1c. The higher magnification BSE-SEM images are placed in the inset



https://doi.org/10.26434/chemrxiv-2024-pggps **ORCID:** https://orcid.org/0000-0002-3194-8561 Content not peer-reviewed by ChemRxiv. **License:** CC BY-NC 4.0

of each figure and their corresponding elemental maps are also shown in Fig. S1 (Supplementary Information S1). The gray contrast regions in the composites belong to the HEB phase whereas the dark contrast regions correspond to the SiC phase. Fragmented distribution of pores can also be located in HBS20 sample between the grain boundaries of the HEB phase and SiC particulates (see Fig. 1b). The pore distribution is a bit different in the case of HBS40 sample. A dense morphology with sparsely distributed pores can be found in Fig. 2b. The SEM-based microstructural observation denotes that the SiC second phase is homogeneously distributed in the composite for HBS20 composite, whereas, in case of the HBS40 specimen, SiC forms a continuous percolating network in the matrix. The corresponding elemental maps shown in Fig. S2 (Supplementary Information S1) reveal the distribution of Ti, Zr, Nb, and Cr elements are reasonably uniform in the matrix phase in the case of the composites.

### 3.2 Fine-scale microstructural analysis

Combined analysis of phase assemblage study and SEM-based microstructural investigation of the composites revealed the discrete presence of HEB phase and α-SiC phase in the sintered microstructure without presence of any identifiable impurity phase. However, the surface of the SiC reinforcement is reported to be covered with a thin layer of $SiO_2$ (Melting point= 1713°C), which may remain undetected. Due to the higher soaking time during the sintering, these may form an intergranular molten phase, thus facilitating the mass transfer during the sintering. Thus, fine-scale microstructural analysis of the bulk sintered composites (Fig. 2 and Fig. 3) is needed to investigate the interfaces and structure of various phases of the bulk samples. The information obtained from finer-scale microstructures can lead to insight into the diffusion-controlled sintering process. Fig. 2a, and Fig. 3a show a typical low magnification HAADF-TEM image of the HBS20 and HBS40 samples respectively, indicating the distribution of different phases in the composite with specific phase contrasts. HEB phase



https://doi.org/10.26434/chemrxiv-2024-pggps **ORCID:** https://orcid.org/0000-0002-3194-8561 Content not peer-reviewed by ChemRxiv. **License:** CC BY-NC 4.0

in the microstructure appears to be bright, whereas the randomly distributed irregular SiC grains appear to be dark. The elemental maps provided in the Fig.S3, Supplementary Information denote homogenous distribution of the elements in the respective phases. A typical bright-field TEM image of HBS20 specimen with a dark-field image shown in the inset is represented in Fig. 2b, showing the presence of HEB grains with tangled dislocations (see the rectangular region marked with a yellow line) giving rise to the contours inside the grain. The microdiffraction pattern was taken from the region (see the inset) and was indexed to confirm the hexagonal HEB phase (space group P6/mmm, a=b= 0.308 nm and c= 0.328 nm). Fig. 2c also shows a low-magnification bright-field TEM image with distinct phase-contrasts of light grey contrast phase indexed to be α-SiC phase ($P6_3/mmc$ space group, a=b= 0.307 nm and c= 0.505 nm). Both the HEB phase and SiC phase own hexagonal crystalline structure, are expected to form high conformity. However, the interface between HEB and SiC phase appears to be incoherent in the HBS20 sample (Fig. 2c), quite a few stacking faults can be observed in the HEB-SiC-interface, indicating the generation of a high amount of stress over the cooling stage due to the difference in thermal expansion coefficients. The HRTEM analysis of the phase boundary of the two adjacent grains (see Fig. 2d) of HEB phase and SiC phase, as is represented in Fig. 2e-g. The IFFT image of the region 1 and region 2 from Fig. 2e is provided in Fig. 2f and Fig. 2g. The phase boundary in Fig. 2e shows a clean interface between the two existing phase (region 1 and 2 belonging to SiC and HEB phase, respectively) without any glassy phase interlayer channels, indicating absence of formation any liquid phase during the sintering. The incoherency of the HEB-SiC interface is due to the crystallographic misfit owing to their large differences in the c-axis length, and due to that no orientation relationship could not be observed. On the contrary, the bright field image corresponding to HBS40 (see Fig. 3b) shows a thick interface between the existing HEB and SiC grain along with occurrence of *in situ* formed carbon as well as glassy phase. The STEM-HAADF image and the corresponding



https://doi.org/10.26434/chemrxiv-2024-pggps **ORCID:** https://orcid.org/0000-0002-3194-8561 Content not peer-reviewed by ChemRxiv. **License:** CC BY-NC 4.0

elemental map is represented in Fig. S4, Supplementary Information. A magnified image of Fig. 3b is displayed on the inset, showing a clear presence of the solidified liquid phase. The composition of the glassy phase is presented in Fig. S4, and it seems that Si, O and C were detected in the EDS spectra from the region. It appears that appropriate circumstances were matched during the sintering for forming strong diffusion bonded interface between HEB and SiC grains through liquid phase sintering mechanism. The micrograph in Fig. 3c indicates the HEB phase along with two adjacent SiC grains. The phase boundary as well as the triple pocket exhibited presence of an amorphous film. A high magnification HRTEM image from the area corresponding to the two-grain interface denoted in Fig. 3c is presented in Fig. 3e. The phase boundary in Fig. 3e indicates a glassy interlayer channel with the typical thickness of 1-2 nm. The IFFT images are presented in Fig. 3e and Fig. 3f can be used to simply deduce the fact that grain boundary is basically a low angle grain boundary. The formation of dislocations in the HEB matrix which can be seen in the IFFT image from the region 2 of Fig. 3f can be due to the thermal stress that is generated due to mismatch in the thermal expansion coefficient as a result of the higher cooling rate during the final stage of sintering cycle.



https://doi.org/10.26434/chemrxiv-2024-pggps **ORCID:** https://orcid.org/0000-0002-3194-8561 Content not peer-reviewed by ChemRxiv. **License:** CC BY-NC 4.0

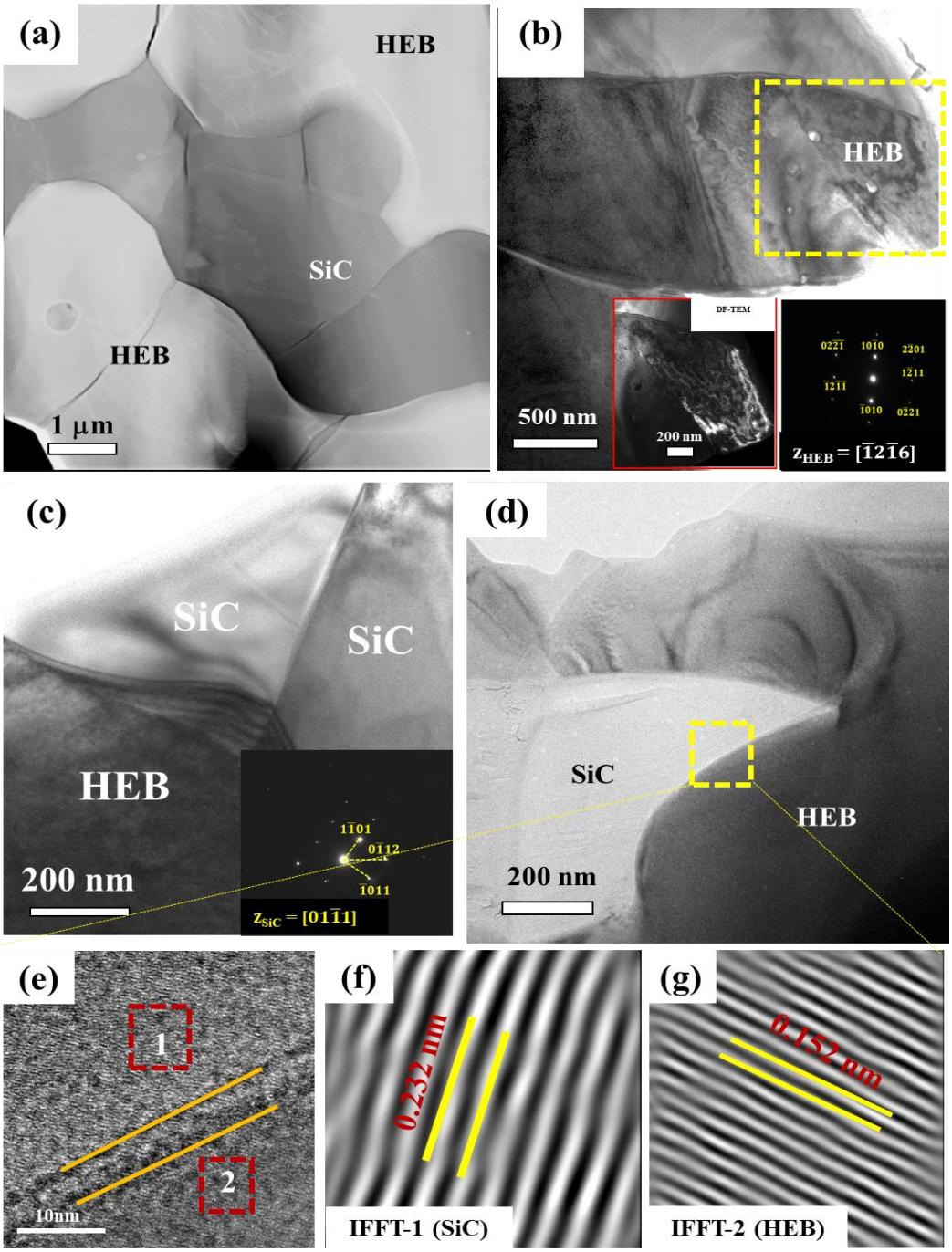


**Fig. 2 (a).** HAADF-TEM image of the HBS20 showing specific phase contrast of the HEB phase and the SiC phase in the fine-scale microstructure. **(b)** Low magnification bright-field TEM image shows grain contours within the HEB phase. The inset exhibits the selected area diffraction pattern (SADP) from the HEB grain within the selected rectangular region indicating the hexagonal structure, Another inset represents a dark-field image of the selected rectangular region. **(c)** A higher magnification bright-field TEM image revealing the formation



https://doi.org/10.26434/chemrxiv-2024-pggps **ORCID:** https://orcid.org/0000-0002-3194-8561 Content not peer-reviewed by ChemRxiv. **License:** CC BY-NC 4.0

of stacking fault in the interface between HEB grain and SiC grain (inset showing SADP from the SiC grain), **(d)** High magnification BF-TEM image showing clean grain boundary between HEB and SiC grains, **(e)** corresponding HRTEM image from the rectangular region (marked as yellow box)**, (f), (g)** corresponding inverse FFT image from the region 1 (SiC phase) and region 2 (HEB phase) respectively.

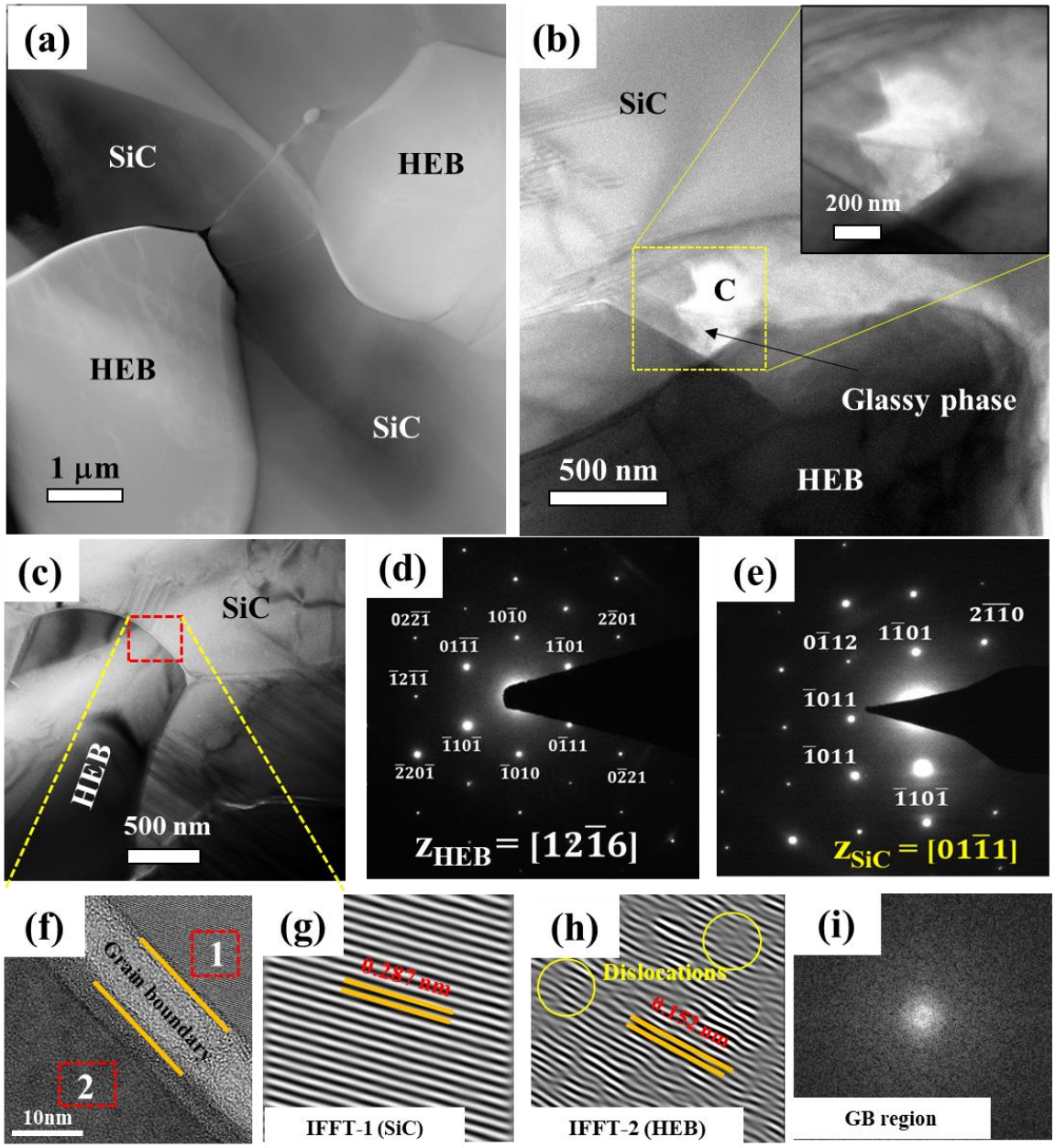


**Fig. 3 (a).** HAADF-TEM image of the HBS40 showing specific phase contrast of the HEB phase and the SiC phase in the microstructure. **(b)** Low magnification bright-field TEM (BF-



https://doi.org/10.26434/chemrxiv-2024-pggps **ORCID:** https://orcid.org/0000-0002-3194-8561 Content not peer-reviewed by ChemRxiv. **License:** CC BY-NC 4.0

TEM) image showing presence of glassy phase near the grain junction of SiC and HEB phase. The inset exhibits the region at higher magnification. **(c)** Another BF-TEM image showing clean grain boundary and a triple grain junction formed between the SiC and HEB grains, higher magnification bright-field TEM image revealing the formation of stacking fault in the interface between HEB grain **(e), (f)** corresponding SAD patterns from the respective phases. **(f)** HRTEM image showing interface region between HEB and SiC grains from the rectangular region (marked as red box in **(e)**), **(g), (h)** corresponding inverse FFT image from the region 1 (SiC phase) and region 2 (HEB phase) respectively.

Two facts arise in the context of the preceding observations: 1) The glassy layer is only present in the composite containing 40 vol% SiC and 2) The state of amorphousness of the phase boundary in HBS40 composite. To elaborate it is necessary to discuss about the formation of glassy phase as well as in situ carbon the thermodynamic point of view first. It is reported that the improved densification due to SiC addition is attributed to the formation of molten intergranular amorphous $SiO_2$ film ($T_m$= 1713°C) that is present on the SiC surface, which synergistically helps in restricting evaporation of any retained $B_2O_3$, present in the boride surface, thus fast mass transfer can occur through a liquid phase sintering mechanism [29]. However, this film formation is greatly dependent on the amount of the SiC phase present in the composite. At lower volume fraction of SiC (here HBS20) in the composite, this $SiO_2$ (which is also present at much lower amount) may also react with SiC, thus forming gaseous SiO phase and carbon, as reported by Nguyen et al. Although the reaction occurs at high temperature (~ 2000°C) at standard condition, this reaction may progress at lower temperatures under the applied pressure in spark plasma sintering (~50 MPa). The produced carbon may participate in another reaction with $SiO_2$ at high temperatures (>1759 °C ) to evolve two gaseous phase: SiO and CO, resulting in further removal of $SiO_2$ from the chamber through vacuum [29]. This matches well with the study by Liang et al., where no interfacial amorphous phase



https://doi.org/10.26434/chemrxiv-2024-pggps **ORCID:** https://orcid.org/0000-0002-3194-8561 Content not peer-reviewed by ChemRxiv. **License:** CC BY-NC 4.0

could not be observed at the $ZrB_2$/SiC interface in a hot-pressed $ZrB_2$–20% SiC composite at 2000 °C [30]. However, in case of the larger volume fraction of SiC in HBS40 composite, it is possible that the further removal of $SiO_2$ may not be completely possible owing to both the lager content of SiC phase (thus, more surface oxide) and lower sintering temperature. Thus, a part of transient liquid phase is likely to be present near the grain which can facilitate liquid state sintering in HBS40 composite. However, no evidence can be found on the crystallization of the transient liquid phase upon cooling. This can be explained from the kinetic viewpoint of the devitrification of glass. As the formed glass is confined in the narrow grain boundary (typically of diameter of 5-10 nm), any volume change during the crystallization incorporates interfacial strain energy, which further increases the nucleation barrier [31-33]. Further, even if crystallization start to occur, the high viscosity of the glassy phase at lower temperature and the confinement in the narrow grain boundary region poses significant kinetic barrier to the crystallization of the glass [32]. Thus, due to the energetically unfavourableness the grain boundary phase stays in the glassy form.

### 3.3 Thermal and electrical conductivity of the sintered ceramics

The thermal and electrical conductivity of the pristine HEB and the composites were calculated as a function of temperature. The room-temperature (RT) thermal conductivity value of the pristine boride (HB) after the porosity correction was calculated to be ~21 W/m. K, which is much lower as compared to conventional $ZrB_2$-based ceramics (~ 72-140 W/m. K at RT) [20]. Consequently, the addition of SiC has been found to have a synergistic effect on the thermal conductivity of the pristine boride matrix as can be seen from Fig. 4a. In the case of both the composite specimens (HBS20 and HBS40), the room temperature thermal conductivity increased to ~22 W/m. K and ~41 W/m. K. Increase in the thermal conductivity by addition of SiC is expected due to the due to the dispersed phase model, as the volume fraction of the higher conductive SiC phase is added in the multicomponent boride matrix. As for the temperature



https://doi.org/10.26434/chemrxiv-2024-pggps **ORCID:** https://orcid.org/0000-0002-3194-8561 Content not peer-reviewed by ChemRxiv. **License:** CC BY-NC 4.0

dependance, the thermal conductivity values of the pristine boride and HBS20 were found to be steadily increasing throughout the measured temperature range (see Fig. 4a). The thermal conductivity of the HEB sample increased from ~21 W/m. K at RT to ~33 W/m. K at 1773K, whereas in case of the HBS20 sample, it increased from ~22 W/m. K at RT to ~39 W/m. K at 1873 K. In contrast, the thermal conductivity of HBS40 reached a maximum value of ~41 W/m. K at room temperature, then further decreased as the temperature increased and finally reaching a minimum value of ~27 W/m. K at 1773K.

The resistivity vs temperature plots for all the compositions are provided in the Fig. S5, Supplementary Information. Electrical conductivity of all the specimens were calculated from the measured resistivity values from RT up to 1073 K with measurements taken every 100K. The room temperature electrical conductivity value of the pristine boride (HB) was calculated to be $1.18\times10^6$ S/m. This is comparable to the typical $ZrB_2$ and $HFB_2$ based UHTC materials which typically shows metallic conduction of ~>$10^5$ S/m that manifests from the dense metal layer in the basal plane of the boride lattices. Intriguingly, addition of SiC in the multicomponent boride was found to have adverse effects on the electrical conductivity. For HBS20 and HBS40, the RT-electrical conductivity values decreased to $0.13\times10^6$ S/m and $0.012\times10^6$ S/m, respectively. The temperature dependance of the electrical conductivity was observed to metallic in nature i.e., as the temperature was increased, the electrical conductivity was found to be decreased in case of all the three specimens, as can be seen from the Fig. 4b. Both SiC-containing composites showed an apparent increase in the electrical conductivity above 873K. From the resistivity vs temperature plots in the Fig. S5 it can be observed that electrical resistivity increased linearly with increasing temperature for the pristine boride samples. However, in the case of the composites, the resistivity decreases linearly as the temperature was increased from the 873K. The dependance of the electrical resistivity on temperature is assessed by the temperature coefficient of resistivity (TCR) values. The TCR



https://doi.org/10.26434/chemrxiv-2024-pggps **ORCID:** https://orcid.org/0000-0002-3194-8561 Content not peer-reviewed by ChemRxiv. **License:** CC BY-NC 4.0

values of all the specimens were calculated from the slope of the resistivity (R) vs. temperature (T) plot using eq. 4; which are listed in Table 2.

$$TCR = \frac{1}{R_{300K}} \frac{dR}{dT} \qquad (4)$$

**Table 2.** Temperature coefficient of electrical resistance (TCR) values of different sintered compositions.

| **Sample Name** | **TCR values ($K^{-1}$)** |
|---|---|
| HB | $4.55\times10^{-4}$ |
| HBS20 | Below 873K: $3.78\times10^{-4}$<br>Above 873K: $-9.41\times10^{-5}$ |
| HBS40 | Below 873K: $3.00\times10^{-4}$<br>Above 873K: $-3.84\times10^{-3}$ |



https://doi.org/10.26434/chemrxiv-2024-pggps **ORCID:** https://orcid.org/0000-0002-3194-8561 Content not peer-reviewed by ChemRxiv. **License:** CC BY-NC 4.0

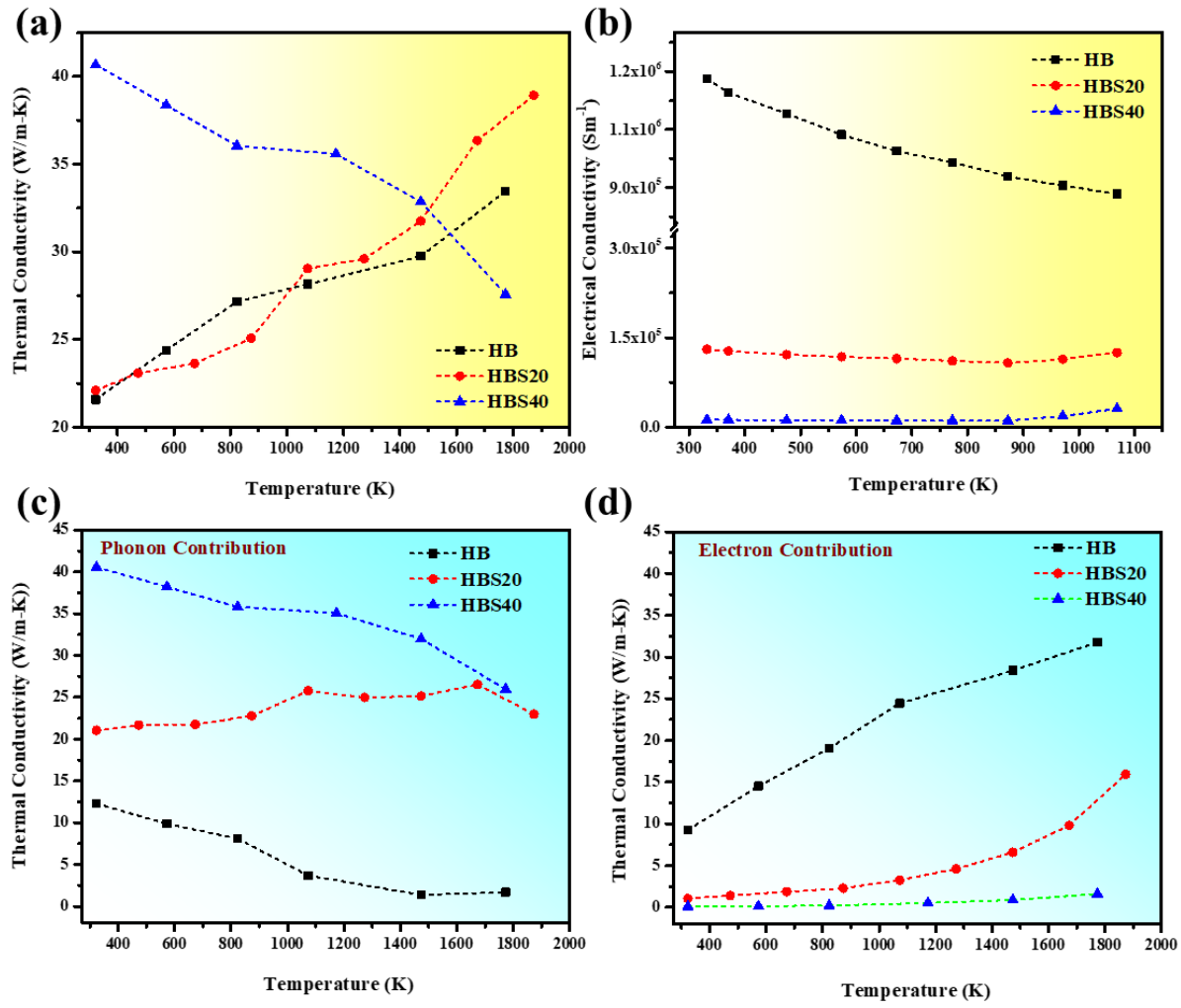


**Fig. 4. (a)** Variation of thermal conductivity of pristine diboride and its SiC based composites at different temperatures. **(b)** Variation of electrical conductivity of pristine diboride and its SiC based composites at different temperatures. **(c)** Phonon contributions of the compositions on total thermal conductivity. **(d)** Electron contributions of the compositions on total thermal conductivity.

The thermal conductivity in the diboride and its composite ceramics is comprised of both the phonon as well as electron contributions. The phonon contribution rises from the semi-ionic/semi-covalent type of bonds (B-B and M-B types) whereas, the electron contribution is manifested from the densely packed metal layers in the basal plane of $AlB_2$-type of lattice. The



https://doi.org/10.26434/chemrxiv-2024-pggps **ORCID:** https://orcid.org/0000-0002-3194-8561 Content not peer-reviewed by ChemRxiv. **License:** CC BY-NC 4.0

electron contribution ($k_e$) of the thermal conductivity can be predicted using measured electrical conductivity ($\sigma_e$), the absolute temperature (T), and the Lorentz constant (L= $2.45\times10^{-8}$ $W\cdot\Omega\cdot K^{-2}$) using the Wiedemann–Franz law (eq. 5). The phonon contribution ($k_p$) can be estimated by subtracting the $k_e$ value from the total thermal conductivity value.

$$k_e = L\sigma_e T \qquad (5)$$

Using the Wiedemann–Franz law, the calculated phonon and electron contribution of the total thermal conductivity values of all the specimens are represented in Fig. 4c and 4d. The $k_e$ and $k_p$ values above 1073K were estimated through extrapolating the linear part of the resistivity vs temperature plot at higher temperature. From Fig. 4c and 4d it can be observed that in case of HB at lower temperature (near RT), the phonon contribution dominates over the electron contribution. However, as the temperature was increased the phonon contribution to the thermal conductivity decreased significantly from ~12.29 W/m.K to ~1.68 W/m.K between 373K and 1773 K; whereas the electron contribution increased steadily from ~9.28 W/m.K to ~31.76 W/m.K. Given the fact that, the phonon contribution originates from B-B and M-B type bonds; in the case of multicomponent systems the phonon contribution is drastically reduced due to increased phonon-phonon interaction (also known as Umklapp scattering), which results from the presence of multiple cations in the cation sublattice and their varying M-B bond lengths. Additionally, at high temperatures the phonon scattering increases significantly, thus reducing the $k_p$ value ~1.68 W/m.K. Furthermore, according to Nordheim's rule for solid solutions as materials with similar electrical resistivity formed solid solution ($NbB_2$, $ZrB_2$, $TiB_2$, $CrB_2$ in our case), the overall electrical resistivity increases due to increased scattering of the electrons by the solute atoms [34]. This additionally results in the reduction of the electron contribution, thus further lowering of the total thermal conductivity at the room temperature. With this explanation above, the reduced thermal conductivity (~21 W/m. K at RT, see Fig.4a) in the pristine boride sample as compared to conventional $ZrB_2$-based ceramics (~ 72-140 W/m.



https://doi.org/10.26434/chemrxiv-2024-pggps **ORCID:** https://orcid.org/0000-0002-3194-8561 Content not peer-reviewed by ChemRxiv. **License:** CC BY-NC 4.0

K at RT) is presumable. However, the TCR value for the HB sample is $4.55\times10^{-4}$ $K^{-1}$, which is much smaller than $3.33 \times 10^{-3}$ $K^{-1}$ (TCR value that is required to have a $\Delta k_e$ of zero i.e. no electronic conduction, as suggested by Zimmermann *et al.* [20]); resulting in an increase in the electron contribution to the thermal conductivity. This is also due to the fact that metal diboride ceramics with the $AlB_2$ structure have 1.33 free electrons per metal ions and the metal ions are arranged in a closed packed basal plane of the crystal structure [35]. This gives rise to increased electronic conduction.

Addition of SiC in the multicomponent boride matrix (here HEB phase) was found to increase the phonon contribution, as can be seen from Fig. 4c. Near RT, the $k_p$ value increased to ~21.05 W/m.K and ~40.56 W/m.K for HBS20 and HBS40, respectively. SiC displays a high rate of phonon transport over electronic conduction [36]. Thus, it is evident that the increased phonon conduction at room temperature originated from the dispersed SiC phase in the HEB matrix. However, with increasing temperature the $k_P$ values of HBS20 were observed not to alter much (from ~21.05 W/m.K to ~22.98 W/m.K) in the temperature range between 373K to 1873K. Whereas, in the case of HBS40, the $k_p$ values were observed to be decreased significantly from ~40.56 W/m.K to ~25.95 W/m.K within the same temperature range. This can be explained from the microstructural point of view as the thermal conductivity is also dependent on the distribution of the second phase in the matrix. In the case of HBS20, the SiC homogeneously distributed in the boride matrix without forming any connected network. Thus, upon increasing temperature the phonon contribution does not significantly drop due to Umklapp scattering within the smaller SiC grains. The smooth interface between HEB and SiC also somewhat facilitates phonon transport, thus raising the $k_p$ to little extent. In contrast, the SiC phase in the HBS40 forms a continuous percolating network, within which the Umklapp



https://doi.org/10.26434/chemrxiv-2024-pggps **ORCID:** https://orcid.org/0000-0002-3194-8561 Content not peer-reviewed by ChemRxiv. **License:** CC BY-NC 4.0

scattering becomes significantly higher and thus lowering the phonon contribution, particularly at high temperature. Although, as the volume fraction of SiC is much higher (where phonon transport is a dominant factor), unlike pristine boride the $k_p$ value did not drop close to zero. Owing to the dominant phonon transport of the SiC phase, it can be seen from Fig. 4d that electron contribution to total thermal conductivity dropped significantly as compared to pristine boride. It is also evident from the TCR values of the HBS20 and HBS40 below 873K, which are $3.78\times10^{-4}K^{-1}$ and $3.00\times10^{-4}K^{-1}$, respectively, which are higher than the TCR values of pristine boride. This results in a decrease in electron contribution below 873K, in case of the composites. At room temperature, $k_e$ values for HBS20 and HBS40 are ~1.05 W/m.K and ~0.097 W/m.K, respectively. This indicates that electron contribution has little to no effect on the overall thermal conductivity of the composites near room temperature. Surprisingly, a sudden rise in the $k_e$ value from ~1.05 W/m.K to ~15.94 W/m.K can be observed from Fig. 4d in the case of the HBS20 composite above 873K. The corresponding TCR value above 873K appears to be negative, which is ~$(-9.41\times10^{-5}K^{-1})$ which indicates an increased electronic conduction due to possible increase in the activation energy for conduction. Earlier studies has reported that, α-SiC (6H-SiC, band gap 3.02 eV) displays an increased activation energy from 01 eV to 0.7 eV in the temperature range of 800 K-1150 K [37]. Following which it is presumable that the increment in $k_e$ value may have occurred due to the increase in the charge carriers in SiC with increased temperature. However, this increment is rather small in the case of HBS40 i.e., from ~0.0974 W/m.K to ~1.61 W/m.K. Due to the continuous network formation in HBS40, the conductivity arises from the bulk SiC where the phonon transport is a dominant mode. Nonetheless, the presence of glassy phase in the HEB-SiC interface (owing to the liquid phase sintering mechanism, see Fig. 3b and 3f) hinders the electron transport at elevated temperature owing to its insulating nature. This leads to an overall decrease in $k_e$ for HBS40 specimen at elevated temperature.



https://doi.org/10.26434/chemrxiv-2024-pggps **ORCID:** https://orcid.org/0000-0002-3194-8561 Content not peer-reviewed by ChemRxiv. **License:** CC BY-NC 4.0

### 3.4 Oxidation behavior at 1400°C

An oxidation study was conducted on the pristine sample as well as the HEB-SiC composite samples to observe the oxidation behavior at a higher temperature. The XRD patterns obtained from all the oxidized sample surfaces during isothermal exposure at 1400°C revealed either or both of the two different complex oxides existing in the oxide layer including $ZrNbO_7$, and $CrNbO_4$ (see Fig. 6) which may have originated from the existing HEB phase. Apart from the existence of a highly crystalline HEB phase, a few peaks of SiC can also be observed from the XRD spectra of the composite samples. The appearance of a broad hump which is a characteristic of the presence of any glassy phase cannot be located in any of the XRD pattern. The principle oxide phases that can be found on the oxidized composite sample surfaces majorly belong to crystalline $SiO_2$. This can be a result of continuous devitrification of glassy or amorphous $SiO_2$ at a higher temperature when exposed for a longer time.

Further cross-sectional microstructural investigation and its corresponding elemental maps of the oxidized samples as represented in Fig. 7 reveal the detailed insight into the oxidation layers inside different samples. For pristine boride sample (HB), the expected oxidation products are mix-oxides and $B_2O_3$. Such similarities can be observed in Fig. 7a. The cross-sectional morphology of the HB sample reveals the presence of a distinct oxidized region across the thickness (~ 440±98 µm). A close observation of the oxidized region reveals dense morphology along with the presence of two different phase contrast. The whitish phase-contrast region belongs to the composite oxides, preliminary containing oxides of Nb, Ti, Zr, and Cr, as can be seen from the corresponding elemental map. The black contrast region may be originated due to the molten $B_2O_3$ phase, which forms during the oxidation of the constituent borides. Boron being difficult to detect in EDS (Energy dispersive spectroscopy), could not be detected



https://doi.org/10.26434/chemrxiv-2024-pggps **ORCID:** https://orcid.org/0000-0002-3194-8561 Content not peer-reviewed by ChemRxiv. **License:** CC BY-NC 4.0

properly. On the other hand, the cross-sectional BSE image of oxidized HBS20 (see Fig. 7b) reveals four different kinds of morphology in the microstructure. EDS elemental map was further employed to identify these four reaction layers. In the cross-sectional microstructure, a distinct two-layer oxide structure was observed. The outer layer (OL) consisted of a $SiO_2$-rich oxide layer, which was followed by a porous inner oxidation layer (IOL) composed of a mixed oxide region. The inner oxidation layer is preliminary consisted of composite oxides of Nb, Ti, and Zr; primarily $ZrNbO_7$ and $SiO_2$. Occasional presence of unoxidized SiC can also be found in the inner oxide layer. The thickness of both the oxide layers were found to be homogeneous throughout the cross-sectional region. The average thickness of the continuous outer oxide layer was found to be 24±5 µm whereas the inner oxidation layer was found be comparatively thicker; approximately 150-170 µm. It is noteworthy to mention that beneath the two-layer oxide structure, a distinct layer of SiC-depleted zone can be observed. The elemental maps reveal a clear demarcation between the oxide layers and the SiC-depletion zone, as Si is entirely absent in the depletion layer. However, presence of oxygen in the depletion zone reveals partial oxidation of the HEB phase in the region. Further beneath the SiC-depleted zone, unoxidized composite containing both the HEB phase and SiC phase can be found. On the contrary, the oxidized-HBS40 sample reveals a somewhat different morphology (see Fig. 7c) as compared to that of the HBS20 sample. Much poorer oxidation resistance is observed in the case of HBS40. The thickness of the oxide layer is found be exceed more than 1mm in some of the cross-sectional regions. Clear boundaries between the existing oxide layers cannot be observed. However, two different oxidation layers can be identified from Fig. 7c and its corresponding elemental map, such as (i) thick outer oxidation layer (OL) (contains a continuous $SiO_2$ layer of grey contrast with occasional occurrence of aggregated mix oxide regions with white contrast); (ii) porous inner oxidation layer containing oxides of Nb, Ti, Zr, and Cr. Some regions with unoxidized SiC can also be observed in between OL and IOL. Very thin (almost



https://doi.org/10.26434/chemrxiv-2024-pggps **ORCID:** https://orcid.org/0000-0002-3194-8561 Content not peer-reviewed by ChemRxiv. **License:** CC BY-NC 4.0

unnoticeable) SiC-depleted zone can be spotted in some places between the oxidized region and unaffected regions. A close inspection of oxidized regions reveals the presence of micrometer-sized pores in the oxidized regions which may have provided a pathway for oxygen to penetrate through the oxide layer and lead to further oxidation of the composite ceramic.

The linear oxidation depth is calculated from the thicknesses of the reaction layers of all the oxidized samples and is represented in Fig. 8a. Much improved oxidation resistance can be observed in the HBS20 sample for which oxidation depth (206.4±18.4 µm/min) is found to be the lowest. In addition to this Fig. 8b shows the hardness profile of the oxidation layers as a function of depth from the surfaces for all the oxidized samples. Each of the points is 30-60 µm away from the surface. A similar trend can be observed from all the hardness profiles. The hardness values are found to fall in much lower ranges (0 to 5 GPa) up to a certain distance from the surface and then followed by an abrupt increment. Lower hardness values can be referred to oxidized regions. The distances at which the peak hardness values are observed are different for each of the samples. The greater the distance from the surface, the greater the thickness of the oxidation layer. The results from the hardness profile well corroborate with the cross-sectional microstructural investigation. In the case of the oxidized-HBS20 sample, the peak hardness value is found at a much lower depth as compared to oxidized-HB, and oxidized-HBS40 samples, matching well with the cross-sectional microstructural investigation. It is worthwhile to mention that, in case of an oxidized-HBS40 sample gradual increment of the hardness values can be observed after 1000 µm depth from the surface. These can be referred to as regions with partially oxidized products along with primarily existing HEB and SiC phases.



https://doi.org/10.26434/chemrxiv-2024-pggps **ORCID:** https://orcid.org/0000-0002-3194-8561 Content not peer-reviewed by ChemRxiv. **License:** CC BY-NC 4.0

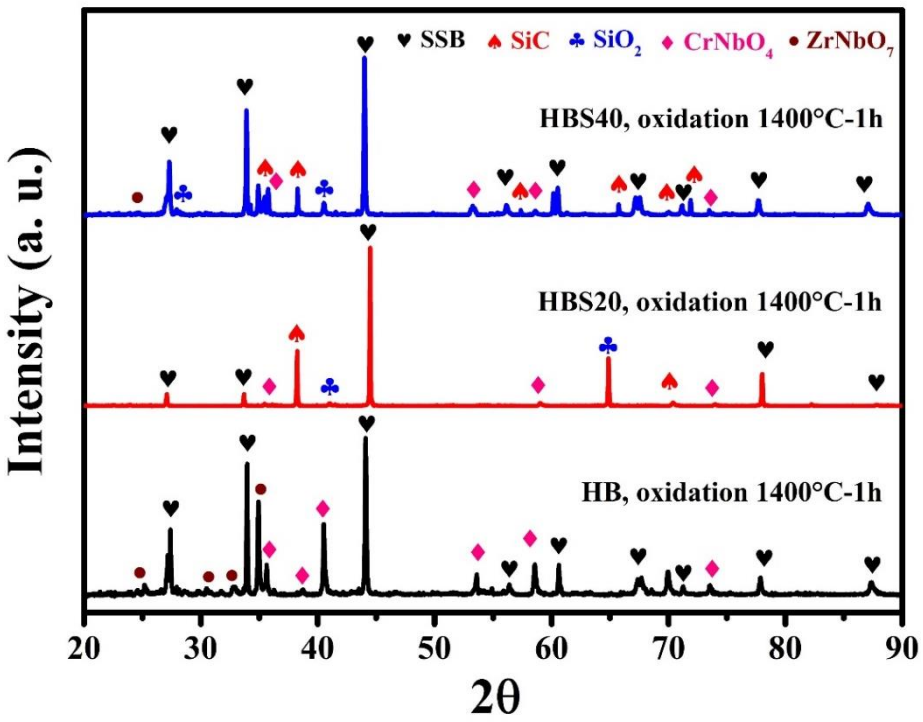


**Fig. 5.** XRD patterns reveal the phase evolution of the sintered compacts oxidized at 1400°C for 1 hour.



https://doi.org/10.26434/chemrxiv-2024-pggps **ORCID:** https://orcid.org/0000-0002-3194-8561 Content not peer-reviewed by ChemRxiv. **License:** CC BY-NC 4.0

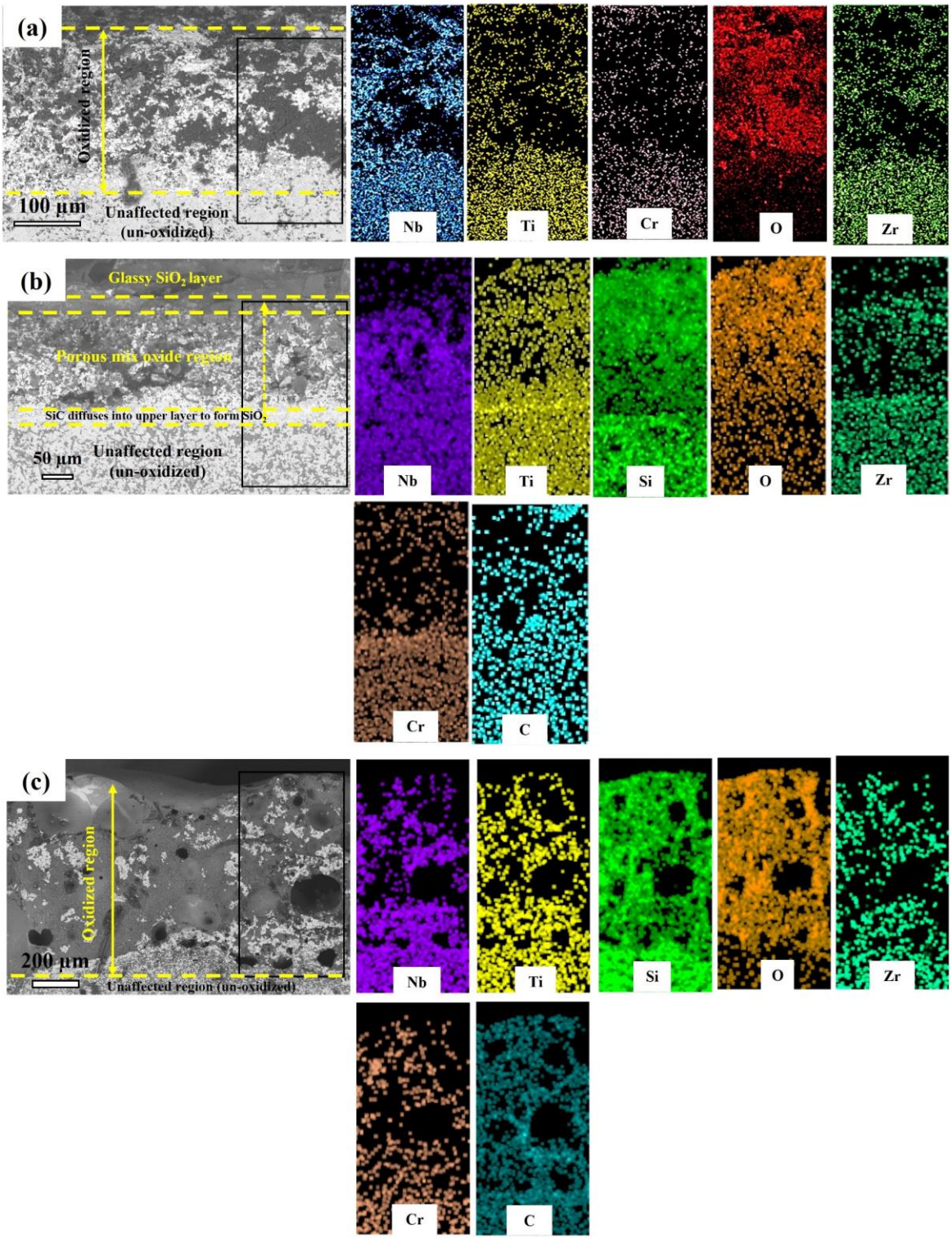


**Fig. 6.** Cross-sectional microstructure and corresponding elemental map revealed different phase-contrast among the oxidation layers in different sintered compacts after oxidation at oxidized at 1400°C for 1 hour. **(a)** HB, **(b)** HBS20, **(c)** HBS40.



https://doi.org/10.26434/chemrxiv-2024-pggps **ORCID:** https://orcid.org/0000-0002-3194-8561 Content not peer-reviewed by ChemRxiv. **License:** CC BY-NC 4.0

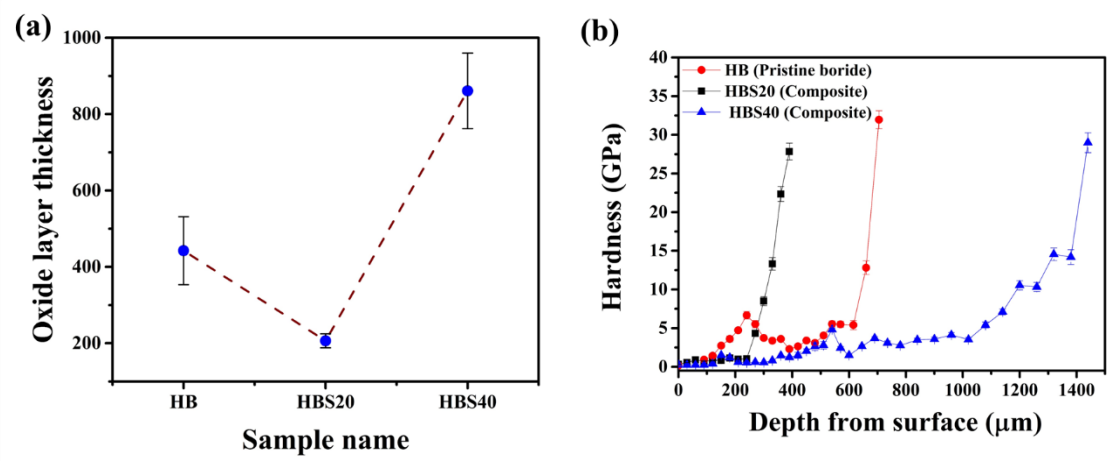


**Fig. 7. (a)** Oxide layer thickness in different sinter compacts after oxidation. **(b)** Measured hardness profile along the cross-sectional region of the oxide specimens.

### 3.5 Arc-jet test of HBS20 composites

Isothermal exposure at 1400°C shows improved oxidation resistance of the HBS20 composite. Thus, in order to investigate the thermo-structural stability of HBS20 composite in the ultra-high temperature regime (>1800°C), Arc-jet test (AJT) has been carried out. The thermal profile of the rise in back wall temperature is shown in Fig. 9a. The gross macroscopic examination of the post arc jet exposure depicted in the inset of the Fig. 9a. shows that HBS20 survived the plasma jet flux of 2.5 MW/m$^2$ for 30 s. No crack or any appreciable erosion can be observed in the front face of the HBS20 sample. However, a few pits can be observed on the surface of the exposed specimen. A cleave was made to observe the macroscopic cross-sectional area which also shows no macroscopic oxide layer, see inset of Fig. 9a. The thermal profile displayed in Fig. 9a shows a steep rise in back wall temperature up to ~668°C within the course of 10 s, and then gradually reaching at maximum 891°C within next 20 s with a decreasing slope. The qualitative changes are not as-such evident from the XRD pattern as shown in the Fig. 9b. Only a minor peak corresponding to $SiO_2$ can be observed in the post-AJT specimen, else no other oxide phases (Oxides of Nb, Ti, Zr and Cr) can be detected. The measured



https://doi.org/10.26434/chemrxiv-2024-pggps **ORCID:** https://orcid.org/0000-0002-3194-8561 Content not peer-reviewed by ChemRxiv. **License:** CC BY-NC 4.0

crystallite size using evaluated using Scherrer's formula (see eq. 10) were found to be increased in the post-AJT specimen from 54±14.5 nm to 76.6 ±16.8 nm, as compared to the unexposed specimen.

$$Crystallite\ size = \frac{0.9\lambda}{\beta cos\theta} \qquad (10)$$

Here, where, $\beta$ is full width at half maximum (FWHM) of individual peak, $\lambda$ is wavelength of incident X-ray, and $\theta$ is Bragg's diffraction angle.

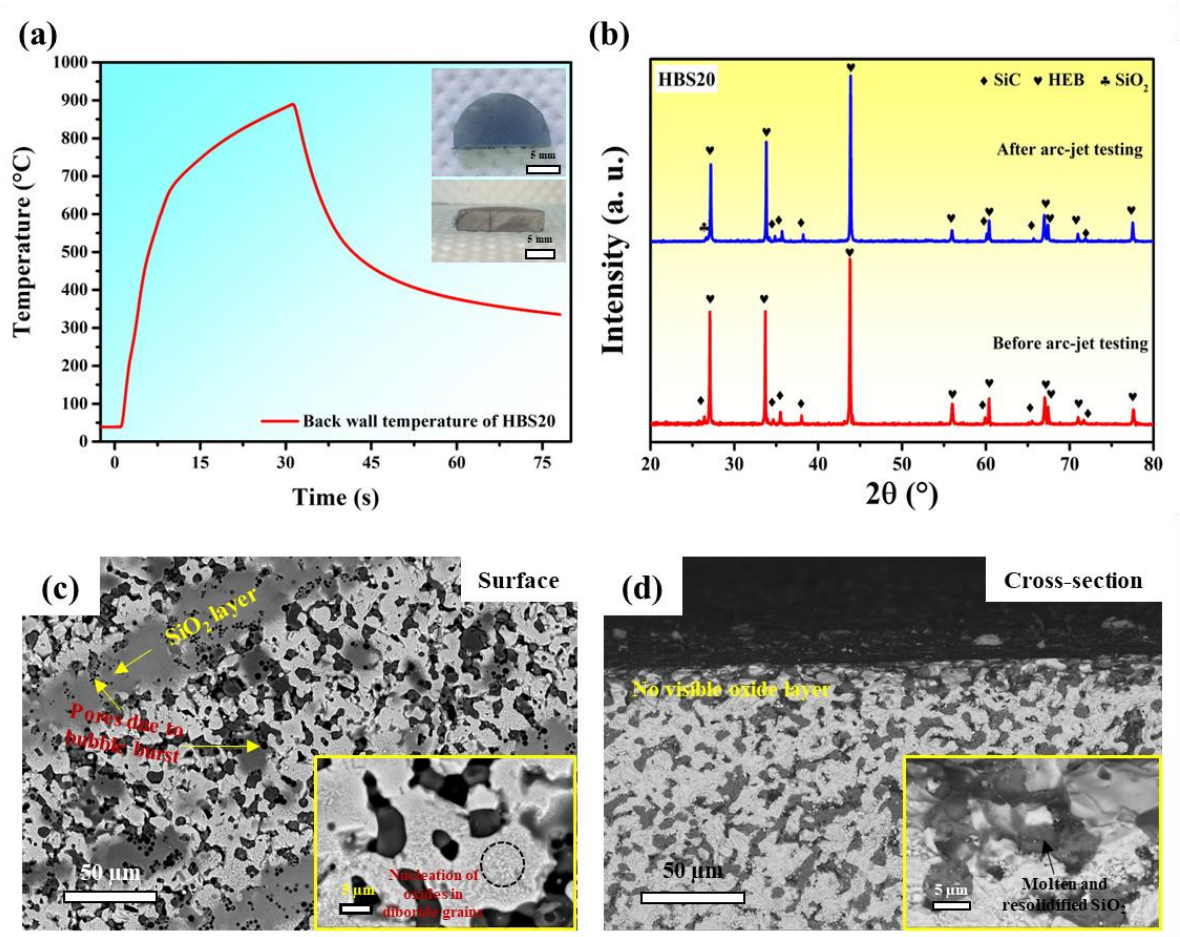


**Fig. 8. (a)** The thermal profile of the arc-jet tested sample HBS20. **(b)** XRD spectra of plasma arc jet exposed HBS20 composites. SEM micrographs of oxidised samples (a) Surface, (b) Cross-sectional are, displaying pits and oxide scale obtained after plasma arc jet exposure.



https://doi.org/10.26434/chemrxiv-2024-pggps **ORCID:** https://orcid.org/0000-0002-3194-8561 Content not peer-reviewed by ChemRxiv. **License:** CC BY-NC 4.0

Fig. 9b shows the BSE-SEM image of the plasma exposed surface. Both the primary phases (boride and SiC) can be observed on the surface along with occasional continuous layer of $SiO_2$. The continuous layering of $SiO_2$ is due the preferential oxidation of SiC, which can be seen to create pores in the interface of HEB ad SiC grain. Multiple pits can be seen on surface of the sample are presumed to be caused by evolution of CO and $CO_2$ escaped gases. These pits can often accelerate the oxidation process by channelling oxygen inside the subsurface area. A high magnification image presented in the inset of Fig. 9b, shows manometer sized oxide nuclei on the diboride grains. EDS elemental map of the high magnification image is presented in Fig. S6a, Supplementary Information which shows the oxygen is present on the whole surface region. On the other hand, the cross-sectional image (Fig. 9c) of the unpolished sample displays no visible oxide layer. Unlike previous oxidation test, no SiC depleted zone can be found within the cross-section. Another high magnification image (see inset of Fig. 9c) from the cross-sectional area indicates traces of melting and rapid solidification of the formed $SiO_2$ (melting temperature ~ 1710°C), which has formed during the plasma exposure. The presences of $SiO_2$ in those region can be confirmed from the EDS elemental maps, as shown in Fig. S6b, Supplementary Information.

### 3.6 Analysis of oxidation behaviour

The oxidation of the pristine HEB as well as SiC-reinforced composite at ~1400°C results in the formation of $B_2O_3$, oxides of the component borides, and $SiO_2$; as observed from the XRD and SEM-based microstructural investigation. Assuming stoichiometric oxidation, the following reactions could be postulated. The Gibbs free energy of the reactions are calculated using FactSage software and presented in Fig. S7, Supplementary Information.

$$2NbB_2 + 5.5O_2 = Nb_2O_5 + 2B_2O_3 \quad \text{(R1)}$$

$$ZrB_2 + 2.5O_2 = ZrO_2 + B_2O_3 \quad \text{(R2)}$$



https://doi.org/10.26434/chemrxiv-2024-pggps **ORCID:** https://orcid.org/0000-0002-3194-8561 Content not peer-reviewed by ChemRxiv. **License:** CC BY-NC 4.0

$$TiB_2 + 2.5O_2 = TiO_2 + B_2O_3 \quad \text{(R3)}$$

$$2CrB_2 + 4.5O_2 = Cr_2O_3 + 2B_2O_3 \quad \text{(R4)}$$

$$SiC + 1.5O_2 = SiO_2 + CO \quad \text{(R5)}$$

The overall temperature regime for oxidation can be divided into two parts: (i) low temperature (~ 700°C to 1100°C), and (ii) intermediate temperature (~ 1200°C to 1400°C). From the microstructural investigation, it can be observed that when pristine diboride is exposed to air at 1400°C, only one layer of an oxidized region can be found over the unaffected areas (see Fig. 7a). At the low-temperature regime (~ 700°C to 1100°C), oxidation of all the constituent borides is spontaneously favorable. The reactions result in the production of molten $B_2O_3$ (melting temperature ~ 500°C). In the outer layer, the molten $B_2O_3$ forms a continuous liquid glassy phase that provides passive protection by limiting oxygen diffusion through the glassy layer. The inner layer mainly consisted of mix-oxides that have formed during the oxidation of the HEB phase. However, in the intermediate temperature region, as the temperature reaches above 1200°C, the vapour pressure of $B_2O_3$ increases rapidly, leading to its rapid evaporation. A porous oxide layer is left behind as $B_2O_3$ evaporates. Meanwhile, at 1400°C when the underlying boride becomes more prone to oxidation, it further formed molten-$B_2O_3$ fills the pores in the mix-oxide regions. This leads to the generation of a dense mix-oxide layer which provides further protection from oxidation at high temperatures. This can be seen from Fig. 7a in the outer region of the oxidized-HB sample, a dense microstructure of the mix-oxide grains can be found with glassy $B_2O_3$ in between them.

On the other hand, the addition of the SiC phase (20 vol%) has been found to reduce the oxide scale compared to nominally pure HB (containing the HEB phase). Similar has been also observed in conventional $ZrB_2$-SiC composites. It has been reported that, in the case of $ZrB_2$-SiC composites, $ZrB_2$ preferentially oxidizes below ~ 1100°C. Temperature above this range,



https://doi.org/10.26434/chemrxiv-2024-pggps **ORCID:** https://orcid.org/0000-0002-3194-8561 Content not peer-reviewed by ChemRxiv. **License:** CC BY-NC 4.0

when $B_2O_3$ evaporates significantly, passive oxidation of SiC begins (as per R5). This results in the formation of a more stable borosilicate layer on the surface providing a protective barrier to oxygen diffusion and slowing down the evaporation of $B_2O_3$, and thus making these composites more resistant to oxidation. During active oxidation of SiC, it transforms into $SiO_2$ from the surface of the grains. Due to its high viscosity (which provides better wettability) and volumetric increase (~ 118%), the transformed $SiO_2$ disperses in grain boundaries in the entire oxide layer on the composite. However, entrapment of CO (g) formed during oxidation of SiC or volatilization of $B_2O_3$ (g) due to higher vapour pressure can also lead to the formation of bubbles in the underlying oxide layer. This can leave cracks or crates in the oxide layer underneath (defined as the inner oxidation layer), as can be seen from the microstructure of both the HBS20 (see Fig. 7b) and HBS40 sample (see Fig. 7c).

One interesting thing to observe is the presence of the SiC-depletion zone beneath the inner oxidation layer (IOL) in the microstructure of the oxidized-HBS20 sample (Fig. 7b). Similar morphology was also observed in $ZrB_2$-SiC composites beneath the $ZrO_2$-$SiO_2$ layer which has formed during oxidation. The formation of inner oxidation creates an oxygen partial pressure gradient across the sample. Under such conditions (i.e. at higher temperature and low partial pressure of $O_2$) SiC undergoes active oxidation by the following reaction,

$$SiC(s) + O_2(g) = SiO(g) + CO(g) \quad \text{(R6)}$$

$$SiO(g) + \frac{1}{2}O_2(g) = SiO_2(g) \quad \text{(R7)}$$

The gases which form at a lower partial pressure of oxygen, get oxidized (as per R7) while moving to the surface where the partial pressure oxygen is higher. The increment of Si content in the outer oxidation zone can be attributed to the convection of Si-liquid flow from the SiC-depletion zone to the outer layer. In this regard, the improved oxidation resistance of HBS20 can be explained by more sluggish oxygen diffusion through the $SiO_2$-rich outer layer



https://doi.org/10.26434/chemrxiv-2024-pggps **ORCID:** https://orcid.org/0000-0002-3194-8561 Content not peer-reviewed by ChemRxiv. **License:** CC BY-NC 4.0

as well as through IOL and SiC-depletion zone. This is similar to the “solid pillars, liquid roof” scale architecture given by Li *et al.* Here the SiC-depleted zone act as a base and the innermost oxide region provides mechanical support for the adhered borosilicate layer.

It is noteworthy to mention that, upon increasing the SiC content to 40 vol%, the HBS40 sample not only exhibits worse oxidation resistance but also does not show the presence of any SiC-depletion zone. Even though a percolating network exists in HBS40, which is necessary to form a SiC-depletion zone through rapid oxidation of SiC, no sign of such a zone can be observed. However, only a thick outer layer of the $SiO_2$-rich zone can be detected (see Fig. 7c). This can be explained by observing the microstructure of the reaction layers in the oxidized specimen. Close observation of the microstructure of oxidized-HBS40 in Fig. 7c reveals the presence of pores in both the oxide layers which can have formed during the bursting of the bubble that forms due to the entrapped CO (g). As the SiC-content increases, the interconnected network between the SiC grains also increase. Furthermore, the glassy phase present in the phase boundary softens and starts to flow at high temperature. Due to that oxygen start to penetrate the grain boundary, leading to severe internal oxidation. With the increased exposed area, the oxidation rate of SiC becomes much higher along which the bubble formation tendency also increases due to the trapped gas. When the partial pressure inside the bubble increases, it ruptures and exposes the underlying material. This allows for increased oxidation in particular regions. As such regions increases, the overall thickness of the $SiO_2$-rich outer layer also increases. Due to the overall increment in the outer layer thickness, the active oxidation of SiC can get prohibited, leading to the non-existence of the SiC-depletion zone in the HBS40 sample.



https://doi.org/10.26434/chemrxiv-2024-pggps **ORCID:** https://orcid.org/0000-0002-3194-8561 Content not peer-reviewed by ChemRxiv. **License:** CC BY-NC 4.0

## 4. Conclusion:

In the present investigation, the influence of the addition of SiC in the self-synthesized HEB powder and its effect on the phase assemblage, microstructure, mechanical properties, and oxidation behaviours are reported. Few observations few conclusions can be drawn:

I. Introduction to SiC-phase in HEB plays a significant role in enhancing the densification of pristine high entropy diboride. A maximum of ~ 98% relative density was achieved in 40 vol% SiC reinforced composite (HBS40). Phase assemblage analysis revealed no noticeable change in XRD peaks of the HEB phase with the addition of the SiC phase.

II. TEM-based fine scale microstructural investigation revealed upon increasing SiC content from 20% to 40%, the HBS40 specimen undergoes liquid phase sintering through a formation of intergranular amorphous $SiO_2$ film. This leads to higher densification in the HBS40 sample.

III. Oxidative property assessment revealed improved oxidation resistance of 20 vol% SiC reinforced composite as compared to other sintered specimens due to the formation of a stable and uniform boro-silicate layer on the outer surface which reduces the oxygen penetration. However, increasing the SiC content further increases the oxidation rate of SiC, thus further increasing the chance of bubble rupture due to the rapid increment of partial pressure of the entrapped gas. This can further lead to exposure of the underlying material, leaving it more susceptible to oxidation.

IV. Plasma arc exposure on HBS20 sample revealed enhanced sustainability on the harsh re-entry environment without undergoing any structural deformity with a maximum rise in back wall temperature of 891°C. Occasionally distributed glassy $SiO_2$-layer have been observed on the surface of the plasma exposed specimen, however, visible oxide layer can not be observed in the cross-sectional microstructure.



https://doi.org/10.26434/chemrxiv-2024-pggps **ORCID:** https://orcid.org/0000-0002-3194-8561 Content not peer-reviewed by ChemRxiv. **License:** CC BY-NC 4.0

# Supplementary figures

## Supplementary Information

### S1. Progress of densification

Fig. S1a displays densification parameter (Ψ) versus sintering temperature for pristine boride (HB) and HEB-SiC composites (HBS20, HBS40) which indicates the progress of densification during spark plasma sintering at 1800°C with a heating rate of 100°C/min and applied pressure of 30 MPa. A similar trend of displacement can be observed during the progress of densification. The densification parameter (Ψ) for all the samples decreases at the initial stage followed by a gradual increment. The initial reduction of densification parameter (i.e. negative displacement which corresponds to expansion here) in the temperature range of 600°C to 1500°C (which varies for different samples) is primarily due to the thermal expansion of the powders as well as the graphite die and punch. The slope of the graph during the initial stage gradually decreases as the temperature increases. The reduction of the slope is attributed to the combined effect of consolidation-shrinkage and thermal expansion. In the final stage, the consolidation dominates, and the densification parameter increases sharply in the temperature range of 1600°C to 1800°C. In case of the pristine high entropy diboride powder, the densification occurs in a reverse manner up to 1530°C. However, the contraction of the powder volume takes place after 1550°C, the overall densification parameter still shows a negative value. This can be attributed to the higher thermal expansion coefficient of the pristine boride powder as well as the presence of the agglomeration leading to coarser powder being sintered. On the contrary, the slope of the densification parameter (Ψ) versus sintering temperature for SiC reinforced composites (HBS20, HBS40) is less steep when compared with that of HB. The effective reduction of the slope signifies the lowering of the effective expansion during the



https://doi.org/10.26434/chemrxiv-2024-pggps **ORCID:** https://orcid.org/0000-0002-3194-8561 Content not peer-reviewed by ChemRxiv. **License:** CC BY-NC 4.0

initial stage. This can be attributed to that the addition of SiC restricts the expansion of the SSB phase during the initial stage. It is noteworthy to mention that the slope of the curve decreases further when the SiC volume fraction is increased from 20% to 40%. The addition of a further amount of SiC leads to further reduction of initial expansion, thus providing enough scope for densification. This is well reflected in Fig. S1b. Upon increasing the SiC carbide content from 20% to 40%, the Ψ increases from 0.71 to 0.92, thus raising the relative density from 92% to 98%. The addition of SiC along with the SSB phase also lowered the shrinkage temperature (1250°C for HBS20, and 1335°C for HBS40) for the composites, thus revealing the potency of the densification enhancer.



https://doi.org/10.26434/chemrxiv-2024-pggps **ORCID:** https://orcid.org/0000-0002-3194-8561 Content not peer-reviewed by ChemRxiv. **License:** CC BY-NC 4.0

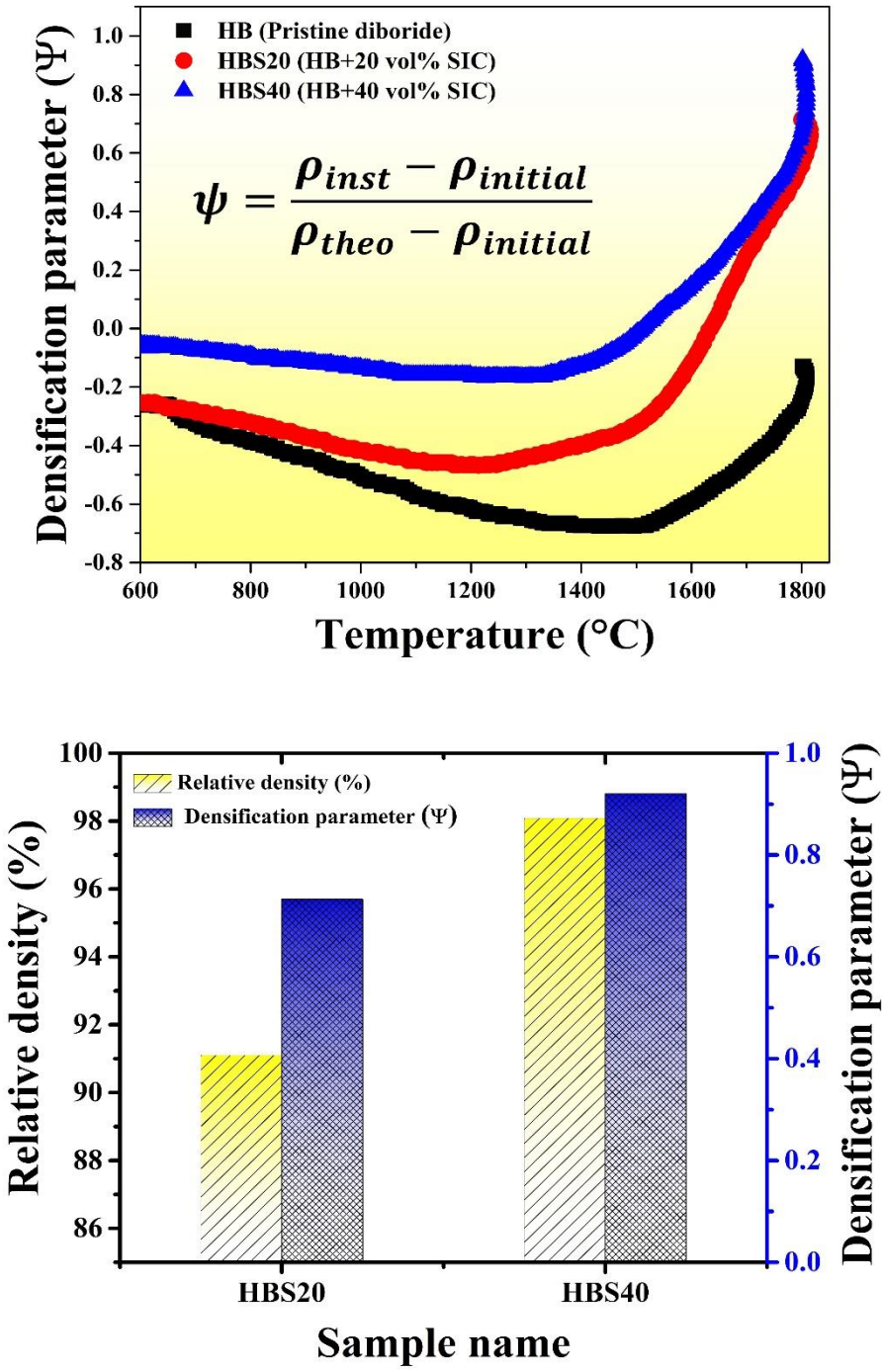


**Fig. S1. (a)** Densification parameter (Ψ) versus sintering temperature for HB (pristine boride) and HEB-x vol% SiC composites (x= 20, 40), sintered using stage spark plasma sintering with a heating rate of 100°C/min and applied pressure of 30 MPa. **(b)** Comparative study of densification behaviors and relative density of the HBS20 and HBS40 compacts.



https://doi.org/10.26434/chemrxiv-2024-pggps **ORCID:** https://orcid.org/0000-0002-3194-8561 Content not peer-reviewed by ChemRxiv. **License:** CC BY-NC 4.0

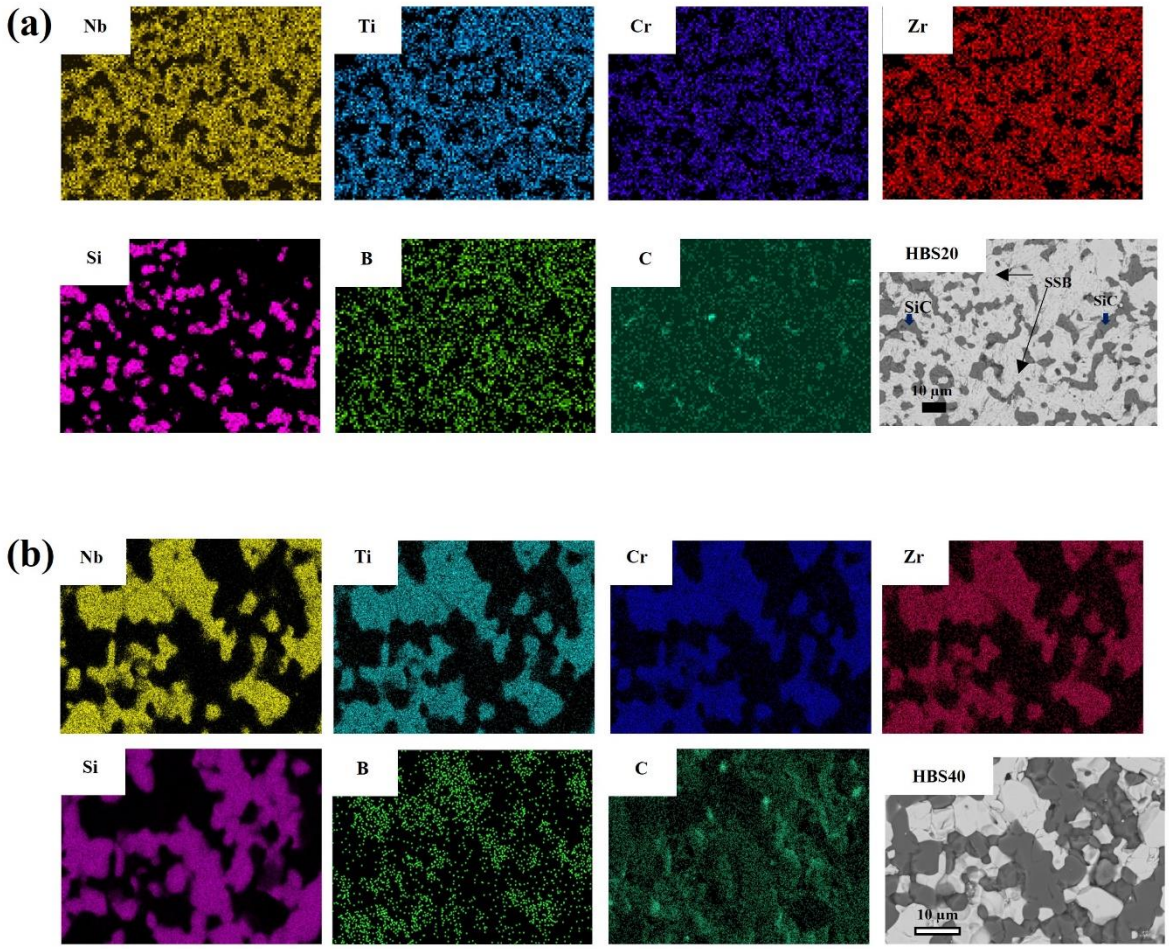


**Fig. S2.** EDS elemental map of HEB-SiC ceramics : **(a)** HBS20, **(b)** HBS40.



https://doi.org/10.26434/chemrxiv-2024-pggps **ORCID:** https://orcid.org/0000-0002-3194-8561 Content not peer-reviewed by ChemRxiv. **License:** CC BY-NC 4.0

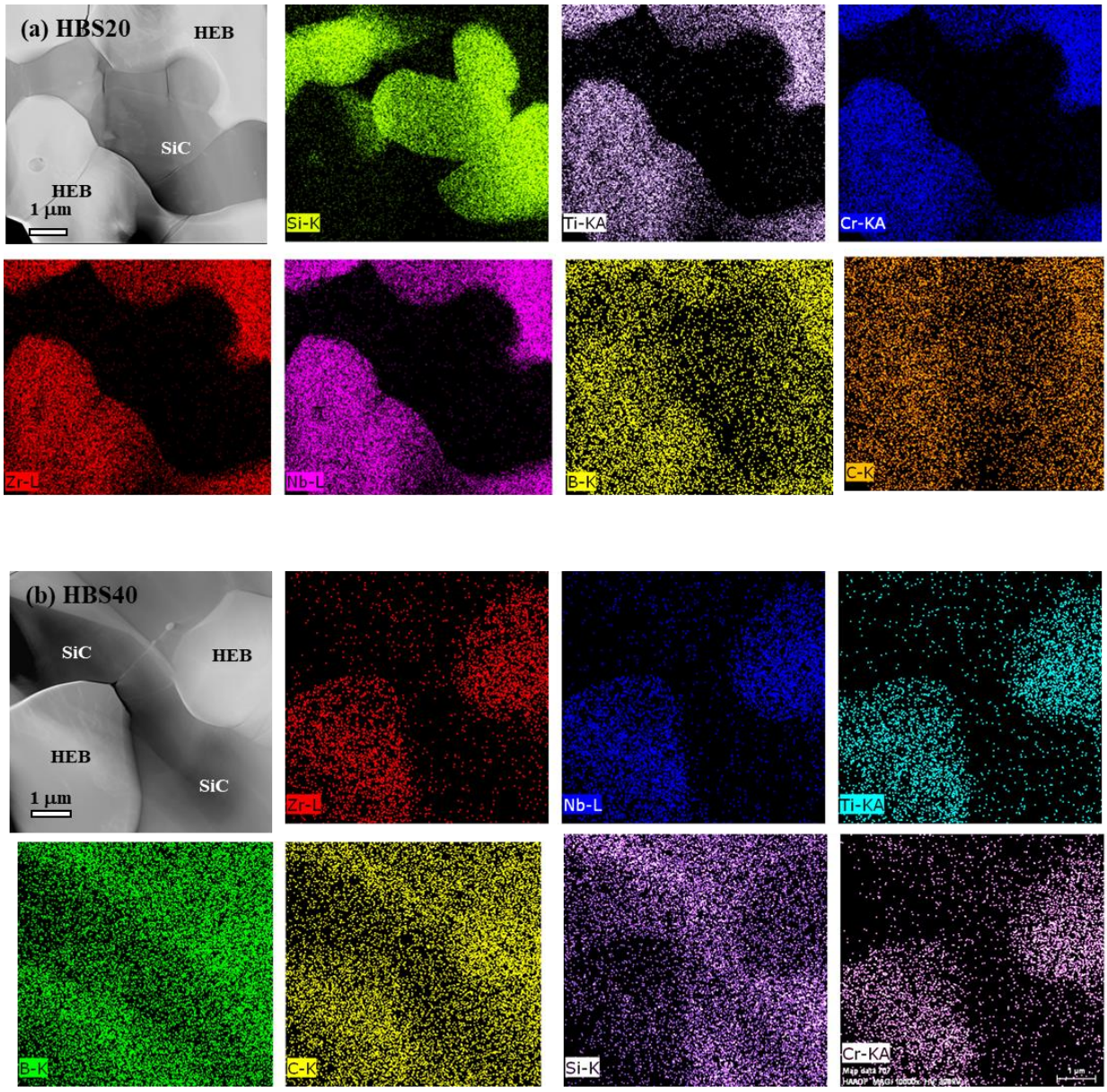


**Fig. S3.** STEM image of the composite samples with the relevant EDS map analysis **(a)** HBS20, **(b)** HBS40.



https://doi.org/10.26434/chemrxiv-2024-pggps **ORCID:** https://orcid.org/0000-0002-3194-8561 Content not peer-reviewed by ChemRxiv. **License:** CC BY-NC 4.0

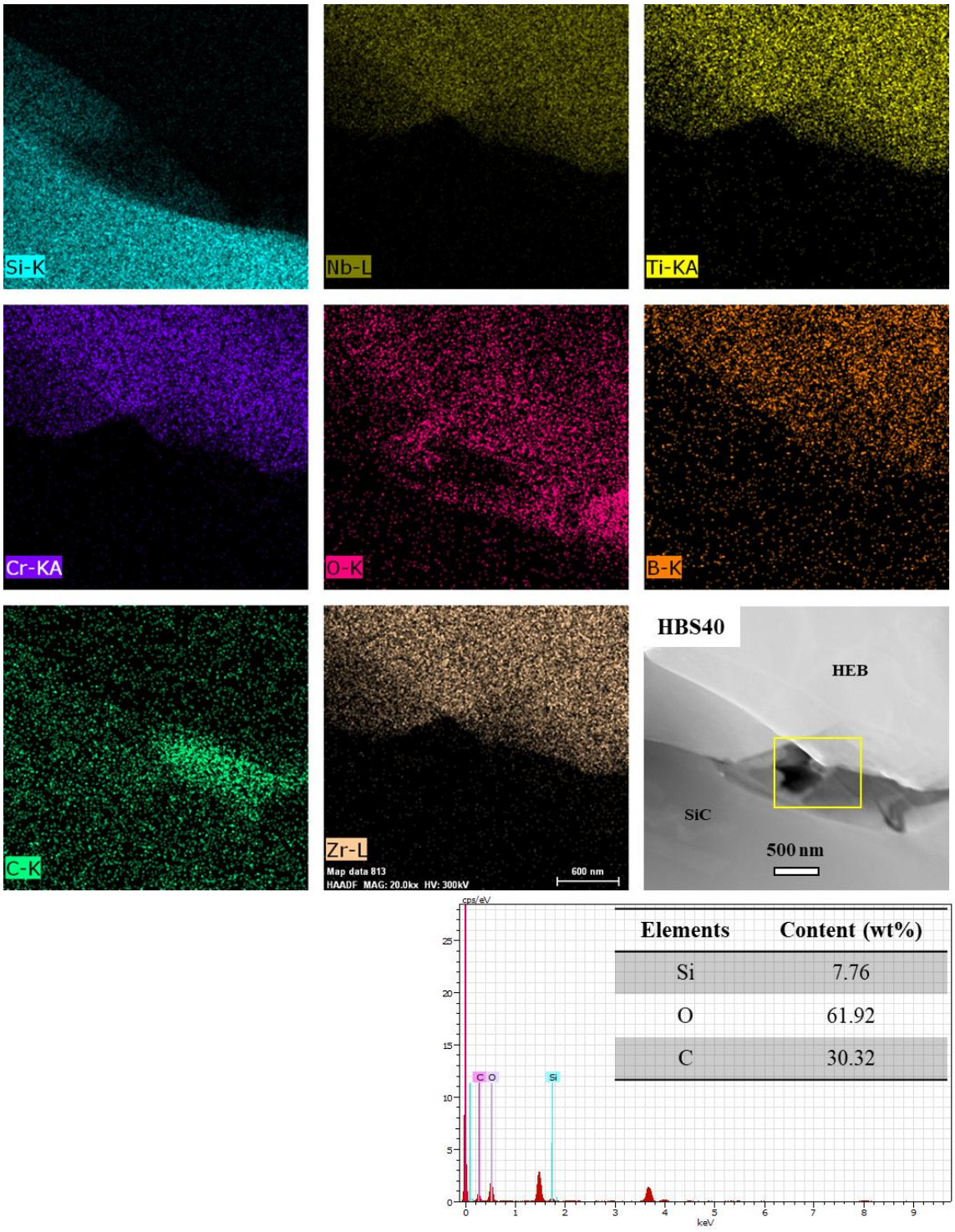


**Fig. S4.** STEM image of the HBS40 with the relevant EDS map analysis showing presence of carbon.



https://doi.org/10.26434/chemrxiv-2024-pggps **ORCID:** https://orcid.org/0000-0002-3194-8561 Content not peer-reviewed by ChemRxiv. **License:** CC BY-NC 4.0

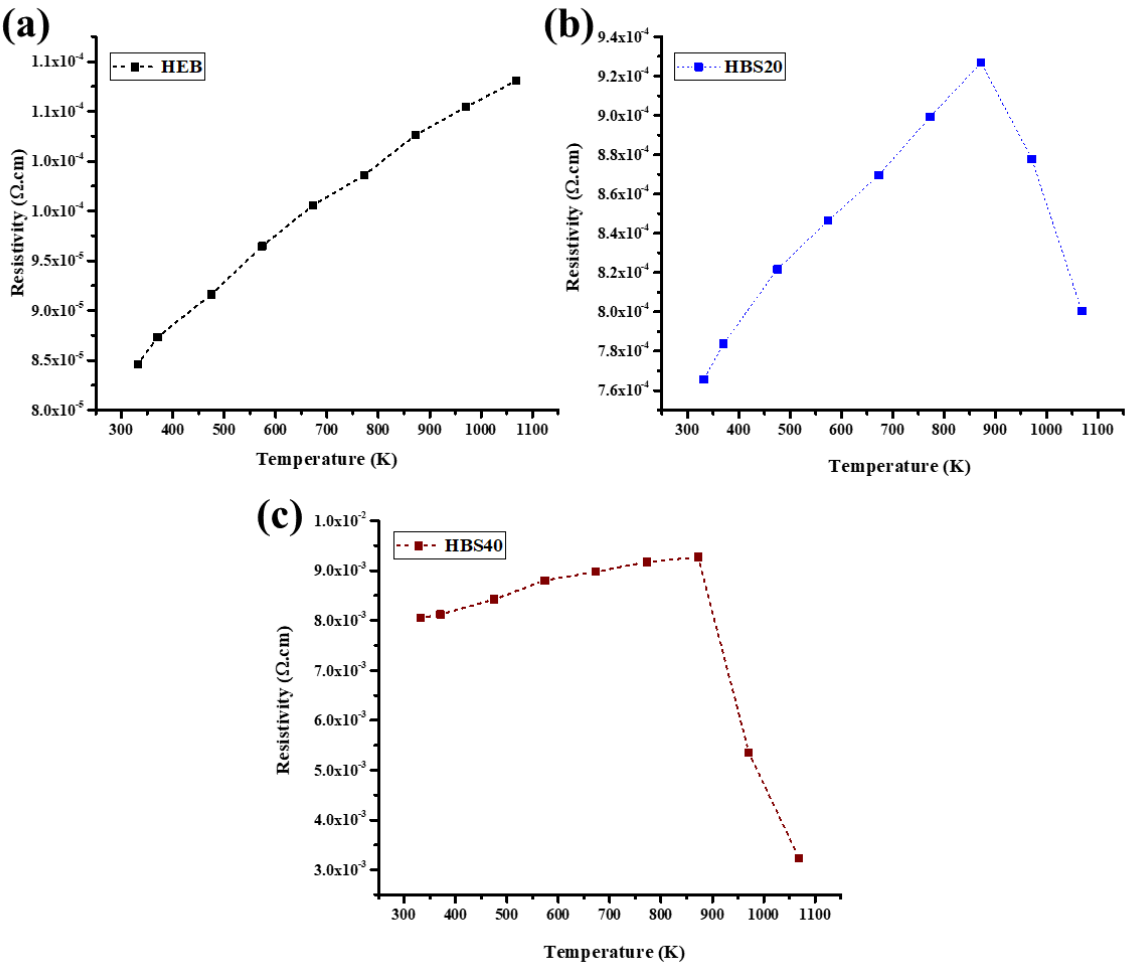


**Fig. S5.** Resistivity vs temperature plots of **(a)** HB, **(b)** HBS20, and **(c)** HBS40



https://doi.org/10.26434/chemrxiv-2024-pggps **ORCID:** https://orcid.org/0000-0002-3194-8561 Content not peer-reviewed by ChemRxiv. **License:** CC BY-NC 4.0

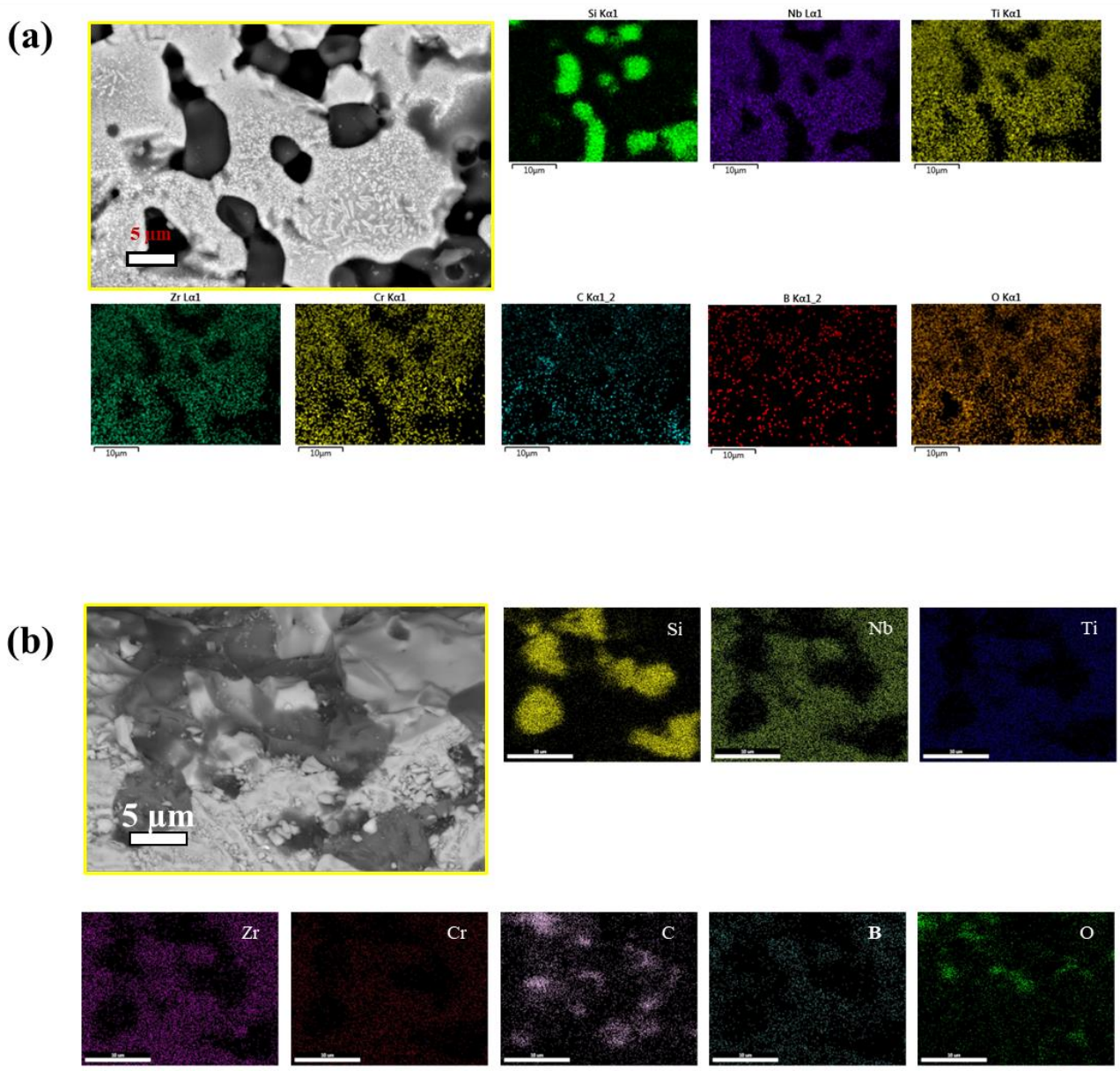


**Fig. S6.** EDS elemental map of HBS20 sample after exposure of Arc-jet testing, **(a)** Surface, **(b)** Cross-sectional area.



https://doi.org/10.26434/chemrxiv-2024-pggps **ORCID:** https://orcid.org/0000-0002-3194-8561 Content not peer-reviewed by ChemRxiv. **License:** CC BY-NC 4.0

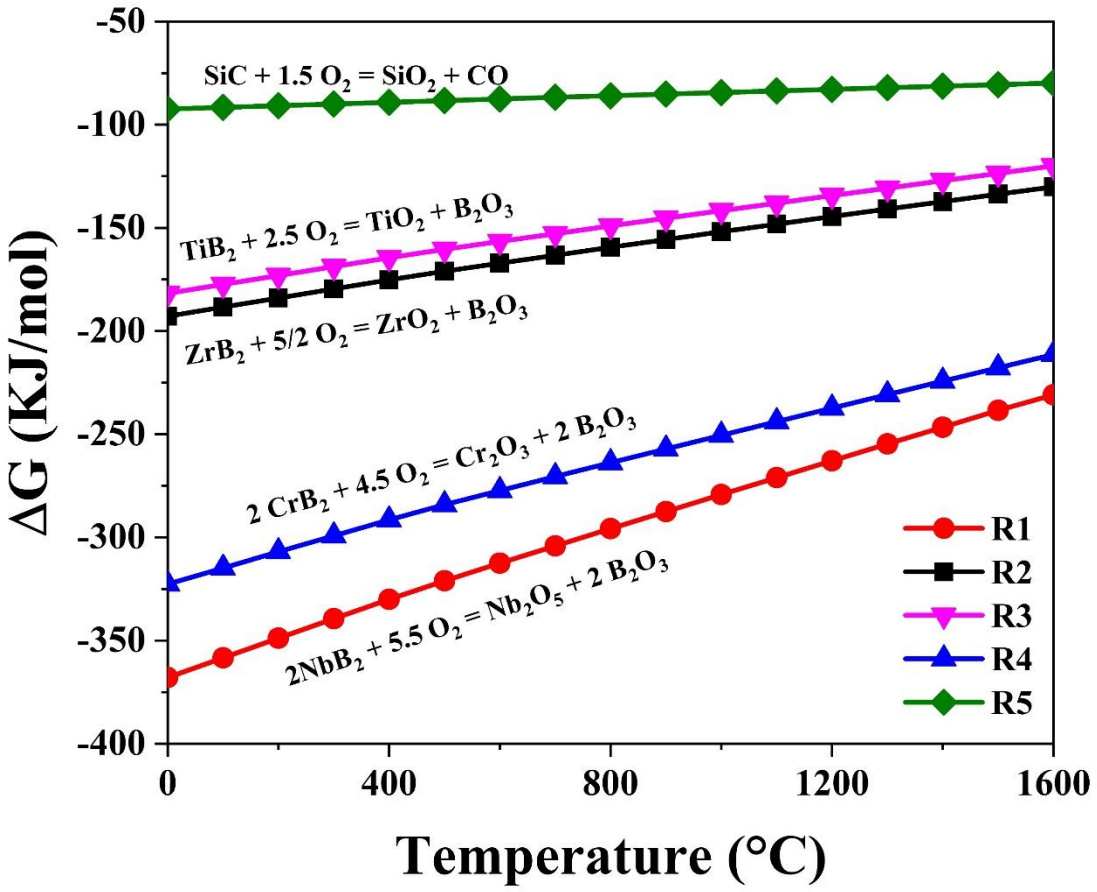


**Fig. S7.** ΔG vs. T plot for the oxidation of the individual components of multicomponent boride-SiC composite system assuming stoichiometric oxidation.



https://doi.org/10.26434/chemrxiv-2024-pggps **ORCID:** https://orcid.org/0000-0002-3194-8561 Content not peer-reviewed by ChemRxiv. **License:** CC BY-NC 4.0

## References

[1] J. Gild, Y. Zhang, T. Harrington, S. Jiang, T. Hu, M.C. Quinn, W.M. Mellor, N. Zhou, K. Vecchio, J. Luo, High-entropy metal diborides: a new class of high-entropy materials and a new type of ultrahigh temperature ceramics, Scientific reports 6(1) (2016) 1-10.

[2] Y. Zhang, W.-M. Guo, Z.-B. Jiang, Q.-Q. Zhu, S.-K. Sun, Y. You, K. Plucknett, H.-T. Lin, Dense high-entropy boride ceramics with ultra-high hardness, Scripta Materialia 164 (2019) 135-139.

[3] Y. Zhang, Z.-B. Jiang, S.-K. Sun, W.-M. Guo, Q.-S. Chen, J.-X. Qiu, K. Plucknett, H.-T. Lin, Microstructure and mechanical properties of high-entropy borides derived from boro/carbothermal reduction, Journal of the European Ceramic Society 39(13) (2019) 3920-3924.

[4] L. Feng, W.G. Fahrenholtz, G.E. Hilmas, Processing of dense high-entropy boride ceramics, Journal of the European Ceramic Society 40(12) (2020) 3815-3823.

[5] Y. Zhang, S.-K. Sun, W. Zhang, Y. You, W.-M. Guo, Z.-W. Chen, J.-H. Yuan, H.-T. Lin, Improved densification and hardness of high-entropy diboride ceramics from fine powders synthesized via borothermal reduction process, Ceramics International 46(9) (2020) 14299-14303.

[6] G. Tallarita, R. Licheri, S. Garroni, S. Barbarossa, R. Orrù, G. Cao, High-entropy transition metal diborides by reactive and non-reactive spark plasma sintering: a comparative investigation, Journal of the European Ceramic Society 40(4) (2020) 942-952.

[7] L. Feng, W.G. Fahrenholtz, G.E. Hilmas, F. Monteverde, Effect of Nb content on the phase composition, densification, microstructure, and mechanical properties of high-entropy boride ceramics, Journal of the European Ceramic Society 41(1) (2021) 92-100.



https://doi.org/10.26434/chemrxiv-2024-pggps **ORCID:** https://orcid.org/0000-0002-3194-8561 Content not peer-reviewed by ChemRxiv. **License:** CC BY-NC 4.0

[8] S. Iwan, K.C. Burrage, B.C. Storr, S.A. Catledge, Y.K. Vohra, R. Hrubiak, N. Velisavljevic, High-pressure high-temperature synthesis and thermal equation of state of high-entropy transition metal boride, AIP Advances 11(3) (2021) 035107.

[9] C. Wang, M. Qin, T. Lei, Y. He, K. Kisslinger, T.J. Rupert, J. Luo, H.L. Xin, Synergic grain boundary segregation and precipitation in W-and W-Mo-containing high-entropy borides, Journal of the European Ceramic Society 41(10) (2021) 5380-5387.

[10] R. Mitra, A. Bajpai, K. Biswas, Machine learning based approach for phase prediction in high entropy borides, Ceramics International 48(12) (2022) 16695-16706.

[11] M. Qin, S. Shivakumar, T. Lei, J. Gild, E.C. Hessong, H. Wang, K.S. Vecchio, T.J. Rupert, J. Luo, Processing-dependent stabilization of a dissimilar rare-earth boride in high-entropy (Ti0. 2Zr0. 2Hf0. 2Ta0. 2Er0. 2) B2 with enhanced hardness and grain boundary segregation, Journal of the European Ceramic Society 42(12) (2022) 5164-5171.

[12] B. Storr, L. Moore, K. Chakrabarty, Z. Mohammed, V. Rangari, C.-C. Chen, S.A. Catledge, Properties of high entropy borides synthesized via microwave-induced plasma, APL Materials 10(6) (2022) 061109.

[13] Q. Zou, H. Gu, Y. Li, Z. Li, P. Liang, Y. Luo, Characterization and analysis of high-entropy boride ceramics sintered at low temperature, Journal of the American Ceramic Society 106(5) (2023) 2764-2772.

[14] R. Mitra, T. Maity, N. Sharma, K. Tiwari, T. Maiti, K. Biswas, Optimal synthesis, fine-scale microstructural characterization, and property estimation of reactive-spark plasma sintered bulk multicomponent (Nb, Ti, Zr, Cr) B2, Journal of Materials Research 38(8) (2023) 2122-2136.

[15] T.G. Aguirre, B.W. Lamm, C.L. Cramer, D.J. Mitchell, Zirconium-diboride silicon-carbide composites: A review, Ceramics International 48(6) (2022) 7344-7361.



https://doi.org/10.26434/chemrxiv-2024-pggps **ORCID:** https://orcid.org/0000-0002-3194-8561 Content not peer-reviewed by ChemRxiv. **License:** CC BY-NC 4.0

[16] X. Zhang, L. Xu, S. Du, W. Han, J. Han, Crack-healing behavior of zirconium diboride composite reinforced with silicon carbide whiskers, Scripta Materialia 59(11) (2008) 1222-1225.

[17] G.B. Yadhukulakrishnan, A. Rahman, S. Karumuri, M.M. Stackpoole, A.K. Kalkan, R.P. Singh, S.P. Harimkar, Spark plasma sintering of silicon carbide and multi-walled carbon nanotube reinforced zirconium diboride ceramic composite, Materials Science Engineering: A 552 (2012) 125-133.

[18] L. Silvestroni, H.-J. Kleebe, S. Lauterbach, M. Müller, D. Sciti, Transmission electron microscopy on Zr-and Hf-borides with MoSi2 addition: densification mechanisms, Journal of Materials Research 25(5) (2010) 828-834.

[19] D. Sciti, L. Silvestroni, G. Celotti, C. Melandri, S. Guicciardi, Sintering and mechanical properties of ZrB2–TaSi2 and HfB2–TaSi2 ceramic composites, Journal of the American Ceramic Society 91(10) (2008) 3285-3291.

[20] J.W. Zimmermann, G.E. Hilmas, W.G. Fahrenholtz, R.B. Dinwiddie, W.D. Porter, H. Wang, Thermophysical properties of ZrB2 and ZrB2–SiC ceramics, Journal of the American Ceramic Society 91(5) (2008) 1405-1411.

[21] M.E. Levinshtein, S.L. Rumyantsev, M.S. Shur, Properties of Advanced Semiconductor Materials: GaN, AIN, InN, BN, SiC, SiGe, John Wiley & Sons2001.

[22] H.-B. Ma, J. Zou, J.-T. Zhu, P. Lu, F.-F. Xu, G.-J. Zhang, Thermal and electrical transport in ZrB2-SiC-WC ceramics up to 1800° C, Acta Materialia 129 (2017) 159-169.

[23] S. Meng, F. Qi, H. Chen, Z. Wang, G. Bai, The repeated thermal shock behaviors of a ZrB2–SiC composite heated by electric resistance method, International Journal of Refractory Metals Hard Materials 29(1) (2011) 44-48.



https://doi.org/10.26434/chemrxiv-2024-pggps **ORCID:** https://orcid.org/0000-0002-3194-8561 Content not peer-reviewed by ChemRxiv. **License:** CC BY-NC 4.0

[24] Z. Balak, M. Azizieh, H. Kafashan, M.S. Asl, Z. Ahmadi, Optimization of effective parameters on thermal shock resistance of ZrB2-SiC-based composites prepared by SPS: using Taguchi design, Materials Chemistry Physics 196 (2017) 333-340.

[25] S.C. Zhang, G.E. Hilmas, W.G. Fahrenholtz, Mechanical properties of sintered ZrB2–SiC ceramics, Journal of the European Ceramic Society 31(5) (2011) 893-901.

[26] X.-Q. Shen, J.-X. Liu, F. Li, G.-J. Zhang, Preparation and characterization of diboride-based high entropy (Ti0. 2Zr0. 2Hf0. 2Nb0. 2Ta0. 2) B2–SiC particulate composites, Ceramics International 45(18) (2019) 24508-24514.

[27] J.-X. Liu, X.-Q. Shen, Y. Wu, F. Li, Y. Liang, G.-J. Zhang, Mechanical properties of hot-pressed high-entropy diboride-based ceramics, Journal of Advanced Ceramics 9 (2020) 503-510.

[28] Y. Zhang, S.-K. Sun, W.-M. Guo, L. Xu, W. Zhang, H.-T. Lin, Optimal preparation of high-entropy boride-silicon carbide ceramics, Journal of Advanced Ceramics 10 (2021) 173-180.

[29] V.-H. Nguyen, S. Ali Delbari, Z. Ahmadi, M. Shahedi Asl, M. Ghassemi Kakroudi, Q.V. Le, A. Sabahi Namini, M. Shokouhimehr, M. Mohammadi, W. Peng, TEM characterization of hot-pressed ZrB2-SiC-AlN composites, Results in Physics 19 (2020) 103348.

[30] J. Liang, Y. Wang, S. Meng, Interface and defect characterization in hot-pressed ZrB2-SiC ceramics, International Journal of Refractory Metals and Hard Materials 29(3) (2011) 341-343.

[31] R. Raj, F.F. Lange, Crystallization of small quantities of glass (or a liquid) segregated in grain boundaries, Acta Metallurgica 29(12) (1981) 1993-2000.

[32] R. Brydson, S.-C. Chen, F.L. Riley, S.J. Milne, X. Pan, M. Rühle, Microstructure and Chemistry of Intergranular Glassy Films in Liquid-Phase-Sintered Alumina, Journal of the American Ceramic Society 81(2) (1998) 369-379.



https://doi.org/10.26434/chemrxiv-2024-pggps **ORCID:** https://orcid.org/0000-0002-3194-8561 Content not peer-reviewed by ChemRxiv. **License:** CC BY-NC 4.0

[33] R. Raj, Morphology and Stability of the Glass Phase in Glass Ceramic Systems, Journal of the American Ceramic Society 64(5) (1981) 245-248.

[34] D.L. McClane, W.G. Fahrenholtz, G.E. Hilmas, Thermal properties of (Zr, TM) B2 solid solutions with TM= Hf, Nb, W, Ti, and Y, Journal of the American Ceramic Society 97(5) (2014) 1552-1558.

[35] M.J. Thompson, Densification and thermal properties of zirconium diboride based ceramics, Missouri University of Science and Technology2012.

[36] J.F. Guria, A. Bansal, V. Kumar, Effect of additives on the thermal conductivity of zirconium diboride based composites – A review, Journal of the European Ceramic Society 41(1) (2021) 1-23.

[37] Y. Taki, M. Kitiwan, H. Katsui, T. Goto, Electrical and thermal properties of off-stoichiometric SiC prepared by spark plasma sintering, Journal of Asian Ceramic Societies 6(1) (2018) 95-101.



https://doi.org/10.26434/chemrxiv-2024-pggps **ORCID:** https://orcid.org/0000-0002-3194-8561 Content not peer-reviewed by ChemRxiv. **License:** CC BY-NC 4.0